Metaball-Imaging Discrete Element Lattice Boltzmann Method for fluid-particle system of complex morphologies with settling case study

Yifeng Zhao (赵益峰)[a,b,c], Pei Zhang (张沛)[b,c], Liang Lei (雷亮)[c], Lingwei Kong (孔令为)[b,c], S.A. Galindo-Torres[b,c,*], Stan Z. Li (李子青)[c,**]

[a]*Collage of Environmental and Resources Science, Zhejiang University, 866 Yuhangtang Road, Hangzhou, 310058, Zhejiang Province, China*
[b]*Key Laboratory of Coastal Environment and Resources of Zhejiang Province, School of Engineering, Westlake University,, 18 Shilongshan Road, Hangzhou, 310024, Zhejiang Province, China*
[c]*School of Engineering, Westlake University, 18 Shilongshan Road, Hangzhou, 310024, Zhejiang Province, China*

Abstract

Fluid-particle systems are highly sensitive to particle morphologies. While many attempts have been made on shape descriptors and coupling schemes, how to simulate the particle-particle and particle-fluid interactions with a balance between accuracy and efficiency is still a challenge, especially when complex-shaped particles are considered. This study presents a Metaball-Imaging (MI) based Discrete Element Lattice Boltzmann Method (DELBM) for fluid simulations with irregular shaped particles. The major innovation is the MI algorithm to capture the real grain shape for DELBM simulations, where the Metaball function is utilized as the mathematical representation due to its versatile and efficient expressiveness of complex shapes. The contact detection is tackled robustly by gradient calculation of the closest point with a Newton–Raphson based scheme. And the coupling with LBM is accomplished by a classic sharp-interface scheme. As for refiling, a local refiling algorithm based on the bounce back rule is implemented. Validations

---

[*]Principal corresponding author
[**]Co-corresponding author
Email addresses: `s.torres@westlake.edu.cn` (S.A. Galindo-Torres), `Stan.ZQ.Li@westlake.edu.cn` (Stan Z. Li (李子青))

on the Jeffery orbit of ellipsoidal particles and three settling experiments of irregular-shaped natural cobblestones indicate the proposed model to be effective and powerful in probing micromechanics of irregular-shaped granular media immersed in fluid systems. The potential of this model on studies of shape-induced physical processes is further investigated with numerical examples that consider the drag and lift forces experienced by realistic particles, as well as the "drafting, kissing and tumbling" process of pairs of non-spherical particles.

1. Introduction

Fluid-particle systems are essential in many human-related operations, including petroleum processing[1], ocean mining[2] and blood circulation[3]. In most cases, the particles involved come in a wide variety of shapes. This makes morphological features a crucial factor in the mechanical analysis of granular materials. The influence of morphologies can be appreciated at different scales producing important fluid disruptions that can be seen at the macro-scale as well as complex interactions between submerged particles at the micro-scale[4, 5, 6]. Taking an example in drug delivery, research[7] shows that the margination and adhesion of drugs in blood vessels are highly susceptible to the drug-particle shape. From the view of experiments, the development of high-resolution imaging has provided a quantitative tool to capture the micro-structure of particles. X-ray Computed Tomography (XRCT) is one of the most prevalent techniques in this area[8]. It enables 3D characterization of the studied material with high resolution. This opens up an opportunity to connect the microstructure of particles with the macro phenomena of fluid-particle systems physically[9, 10, 11]. However, how to accurately simulate the impact of morphological features is still a challenge[12]. Difficulties exist in converting the 3D XRCT images into a quantitative descriptor of morphology. In other words, complex shape features need to be compressed into a concise geometric representation. Moreover, the paradigm to probe mechanical behavior is also an indispensable component, which translates the shape descriptor into a quantitative analysis tool for particle kinematics.

To model particle motions with complex shapes, there are basically two

2

camps: the assembly paradigm and the avatar paradigm[13]. The main difference between them is how to characterize the morphological features. Once the shape is properly represented, collision detection and force calculation follow similar strategies. The assembly paradigm fits shape characteristics by clustering simple, regular graphics like spheres. For example, the sphere-clustering technique is a widely used assembly paradigm due to its simplicity[14, 15, 16]. It approximates the real shape by combining multiple overlapping spheres. Polyhedrons[17], Ellipsoids[18, 19] and Sphere-polyhedrons[20, 21, 22, 23] are also used under a similar clumping framework. However, a large amount of prime graphics (For instance hundreds or thousands of triangular mesh elements as reported in the literature [15, 21]) are needed to achieve sufficient accuracy for characterization of complex shapes especially smooth ones, which leads to a significant increase in contact detection times. This could make simulations time-costly and limit the number of involved particles. To alleviate the efficiency problem, attempts have been made on improvement of the prime graphic[24] and the contact algorithm[25]. But those advances still suffer from artificial surface roughness[26, 27, 23].

The avatar paradigm overcomes the above dilemma by utilizing a uniform mathematical representation as the shape describer, which brings a great advantage in morphological characterization and contact detection. For instance, Kawamoto et al[28] apply the level-set function in the handling of shape capture and contact detection. The proposed level-set approach achieves simulation on thousands of realistic particles reconstructed from XRCT images. The main drawbacks of it are the function interpolation and the lookup mechanism for contact detection[29], which leads to a heavy reliance on computer memory and performance. The superquadric-based method is another interesting implementation[30, 31, 32]. It uses an extension of spheres and ellipsoids as the shape descriptor, which enables particles smooth-surfaces in simulation. But such shape expression has poor applicability for near-spherical particles[33]. This impasse is broken by upgrading it from superquadric to poly-superellipsoid functions [29, 34]. A poly-superellipsoid is an assembly of eight separate superellipsoids, which makes it capable of characterizing more types of convex particles. The implementation of it is also more straightforward than level sets, creating create advantages in dealing with particle motions and contact detection. However, poly-superellipsoid function still has some constraints on the expressed shape for now, such as symmetry and complexity[30, 33]. This could limit their use in more complicated issues, like simulations consisting of concave sands. The

3

aforementioned studies mainly focus on particle-particle and particle-wall interactions. To the best of author's knowledge, few of them have applied such sophisticated geometric representations in DEM simulations coupled with Computational Fluid Dynamics schemes. Thus, although remarkable progress has been made in morphological characterization, it is still a challenge to integrate realistic shapes with micro-mechanical models for probing fluid-particle interactions.

Therefore, there is still a gap in modelling realistic particle morphology with a balance between simulation accuracy and computational efficiency for fluid-particle systems. In this paper, we propose an efficient avatar paradigm called Metaball-Imaging Discrete Element Lattice Boltzmann Method (MI-DELBM), which has the ability to fully consider the morphological factors, especially the smooth and round features, in fluid-particle simulations. For characterization of realistic particles, the Metaball function[35] is modified and adopted as the uniform geometric descriptor. In visualization, Metaballs are n-dimensional isosurfaces. This property enables it to represent a variety of smooth, continuous surfaces, bringing advantages in shape characterization. The main innovation in this paradigm is the Metaball-Imaging algorithm, which can characterize the morphology of particles directly from XRCT images in high-resolution. This enables convincing quantitative study on shape factors and the coupled mechanical model to capture the impact of irregular shapes accurately. For probing the micro-mechanics of involved particles and fluid, a coupled Discrete Element Lattice Boltzmann Method (DELBM) is utilized. Validations show that the proposed MI-DELBM can handle complex morphologies of realistic particles in high-fidelity while infer inter-particle contact forces as well as other related quantities accurately and efficiently.

The contents of this paper are structured as follows: Section 2 is the collection of computational techniques used in this paper, which consists of three parts. Section 2.1 reveals the definition and properties of the used geometric descriptor. Section 2.2 presents a robust algorithm to characterize complex morphologies directly from XRCT images of realistic granular materials. The coupled algorithms for Metaballs to DELBM are briefly stated in Section 2.3. Section 3 demonstrates the validation of the proposed paradigm with simulations on the Jeffery orbit, and three settling experiments of different irregular-shaped cobblestones. The potential of MI-DELBM in study of shape impact is explored with numerical examples on the the drag and lift forces acting on realistic particles, as well as "Drafting, Kissing and Tum-

4

bling" (DKT) process of non-spherical particles in Section 5. In the end, Section 6 summarizes the major contributions from the present work.

2. Methodology

2.1. The Metaball Function

The Metaball function is a shape descriptor for arbitrary shaped particles[36]. It can express interested morphological features by an analytic form:

$$f(\boldsymbol{x}) = \sum_{i=1}^{n} \frac{\hat{k}_i}{(\boldsymbol{x} - \hat{\boldsymbol{x}_i})^2} = 1 \qquad (1)$$

where $\boldsymbol{x}$ represents the input of position; $\hat{\boldsymbol{x}_i}$ is the position of control point i, governing the skeleton of the represented model; n is the number of control points in this Metaball function; $\hat{k}_i$ is the positive coefficient determines the influence scale of i th control point. By setting this function equal 1, the point $\boldsymbol{x}$ is at the contour of the represented particle surface.

The Metaball is an assembly of n-dimensional isosurfaces. It has no additional constraints on control points or weights, which brings it a strong applicability. Both simple and complex shapes, even with round features or concave voids, can all be properly represented. It is worth noting that the value range of the Metaball function with random input is from 0 to ∞. To exemplify these advantages, a 2D Metaball is shown in Figure 1. The function value will be exactly 1 at the surface, with lower values signaling points outside the particle and higher values for points inside. This property is crucial in the definition of loss function for the gradient search (GS) in Metaball-Imaging, which is dedicated to generating a parametric representation of the real shape (Section 2.2.2). Furthermore, this offers simple algorithms to solve the point-inside-particle problem and the collision-detection task between DEM Metaballs. It also gives a straightforward strategy for coupling it with CFD techniques such as LBM (Section 2.3), which brings advantages in efficiency.

2.2. The Metaball-Imaging Algorithm

Here we design a Metaball-Imaging (MI) algorithm to to transform the XRCT image of irregular-shaped particle into an explicit, Metaball-function based mathematical representation, which is called *avatar* in this paper. The

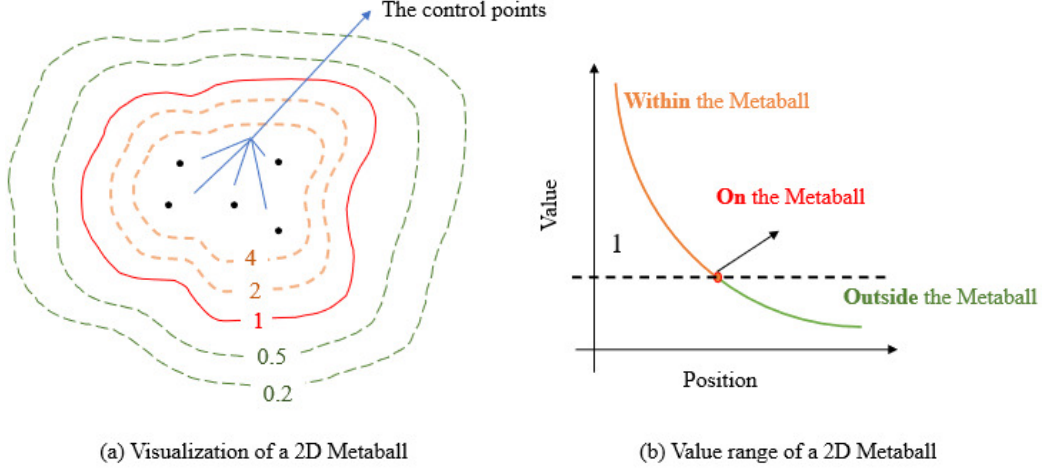(a) Visualization of a 2D Metaball   (b) Value range of a 2D Metaball

Figure 1: The visualization and value range of a 2D Metaball.

avatar possesses high-resolution morphological features and can feed the particle characterization into simulations.

This task can be simplified into an optimization problem, searching for the set of parameters $\{\hat{k}_i, \hat{\boldsymbol{x}_i}\}$ for a Metaball model which can minimize the following function:

$$\arg\min_{\hat{k}_i, \hat{\boldsymbol{x}_i}} \left(\sum_{i=1}^{n_1} \sum_{j=1}^{n_2} \frac{\hat{k}_i}{\left(\boldsymbol{x}_j - \hat{\boldsymbol{x}_i}\right)^2} - 1 \right)^2 \tag{2}$$

where $\{\hat{k}_i, \hat{\boldsymbol{x}_i}\}$ is the parameter set of the targeted Metaball model; $\boldsymbol{x}_j$ stands for the input, coordinates of hull points from XRCT; n_1 and n_2 refer to the number of control points and input samples seperately.

Genetic Algorithm and Gradient Search are two commonly used optimization techniques for engineering problems[37], and in this work will be used to solve Eq. 2. The Genetic Algorithm (GA) is a typical meta-heuristic algorithm, which refers to a series of paradigms consisting of strategies to develop a heuristic answer to an optimization problem[38]. It mimics the process of natural selection from a certain population. This brings it an excellent global search ability and strong robustness. GA can always achieve an optimal solution without any initial values through enough iterations, while the consuming time can be very high for complex problems. The Gradient Search (GS) is a branch of gradient-based algorithms, which can dis-

6

SOIR   TOC

(a) Data Preprocessing   (b) Capturing the principal   (c) Refining the distilled
                              outer contour with GA   outer contour with GS
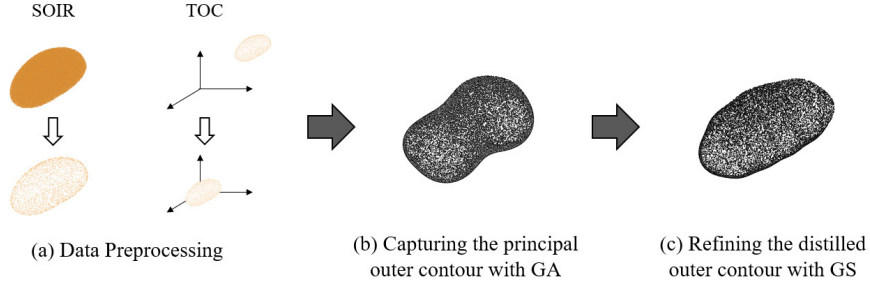
Figure 2: The algorithm flow of the Genetic-based Gradient Search algorithm.

till solutions for optimization problems by gradient of a designed objective function[37]. It originates from Gradient Descent, an efficient search strategy for local optimal solutions. GS shows excellent performance in local search with satisfying speed, while suffering from limited global search ability and strict demand for initial value.

The proposed Metaball-Imaging algorithm is a combination of GA and GS, which makes the best use of their advantages and bypasses those disadvantages. In this scheme, GA is utilized to capture the principal outer contour of the targeted XRCT cloud points, searching for a sufficiently good global solution. And the obtained solution will serve as the initial value for GS. Then, GS can refine the obtained outer contour, filtering out the optimal solution by the gradient relationship. Due to the properties of meta-heuristic and gradient-based algorithms, such a framework can achieve advantages in not only accuracy but also efficiency. The proposed algorithm involve three steps as shown in Figure 2.

Step 1: Data preprocessing of the XRCT cloud points (Figure 2 a). This preprocessing consists of two operations, the specification of interested regions (SOIR) and the transformation of coordinates (TOC). SOIR is to specify those points on outer contour from the XRCT result. This is because the fitting of the Metaball only requires the point hull. TOC is implemented to translate the specified region of interest into the coordinate system centered at the origin. Such an operation can avoid abnormal fitted parameters caused by XRCT coordinates. The point hull obtained through SOIR and TOC is noted as $\boldsymbol{H} = \{Hx_i, Hy_i, Hz_i\}$ ($i \in [1, m]$, where m represents the number of hull points).

Step 2: Capturing the principal outer contour with GA (Figure 2 b). Due

7

to GA's defect in local search and efficiency, it is hard for GA to distill a fine outer contour within an acceptable time. Considering the superiority of GA in global search, the ability to locate the range of the optimal accurately, it is used to capture the rough outer contour, i.e. a sufficiently good solution for Eq. 2. The obtained contour then serves as the initial value in Step 3 for further refinement. It is worth noting that the point hulls in (b) and (c) of Figure 2 are only for visualization. The obtained models are actually presented by Metaballs in this algorithm.

Step 3: Refining the distilled outer contour with GS (Figure 2 c). GS has advantages in local search and efficiency. But its result can be easily affected by the initial value. Thus, GS is implemented to do further refinement on the principle contour distilled by GA, searching for the optimal solution for Eq. 2. In this step, iterative calculations will be carried out based on the gradient relationship. Finally, a refined contour model will be obtained.

Step 2 and 3 will be discussed at length in Section 2.2.1 and 2.2.2. All definitions are introduced in 3D forms, while they also work for 2D cases through expansion.

2.2.1. Genetic Algorithm for capture of the principal outer contour

In the capture of principal outer contour by GA, five segments are included: *population initialization, mutation, crossover, evaluation* and *selection.* Generations of these segments will be carried out as shown in Algorithm 1.

Population Initialization: This process refers to the initialization of N individuals as a population. Each individual represents a possible parameter set $\boldsymbol{M} = \{M_{k_i}, M_{x_i}, M_{y_i}, M_{z_i}\}$ ($i \in [1, n]$) to the fitted Metaball model (See Figure 3). An individual consists of a series of strings defined as Genes, standing for a certain parameter in the set. The number of genes in each initialization is set to be a constant.

In this segment, all individuals are randomized with control points inside targeted point hull H. Such an operation is to satisfy the geometric constraint of the Metaball. The judgment of whether a point P is inside H is completed by linear programming. This problem is defined as the following:

$$\begin{aligned} \underset{A}{\text{Minimize}} \quad & \boldsymbol{CA} \\ \text{Subject to} \quad & \boldsymbol{H}^T \boldsymbol{A} = \boldsymbol{N}^T \end{aligned} \tag{3}$$

Algorithm 1 The Genetic Algorithm for capture of the principal outer contour

Input: the preprocessed point hull $\boldsymbol{H}$, the number of generations E^{ga}, the number of individuals in the population N_I, the number of genes in each individual N_G, the mutation coefficient C_m, the crossover coefficient C_c.

Output: the Metaball model of the principal outer contour $\boldsymbol{M}^{ga}$.

1: **Initialization -** N_I individuals are randomly initialized with a string of N_G genes. The control points in each individual are set to be inside $\boldsymbol{H}$;
2: **for** $i = 1, 2, ...,$ to E^{ga} **do**
3:     **Mutation -** For each indivudial, performing muatation with coefficient C_m;
4:     **Crossover -** For random pair of individuals, performing crossover with coefficient C_c;
5:     **Evaluation -** For each individual, calculating the fittness score;
6:     **Selection -** Selecting the fittest N_I individuals for next generations;
7: **end for**
8: **Return:** The fittest individual in the population $\boldsymbol{M}^{ga}$.
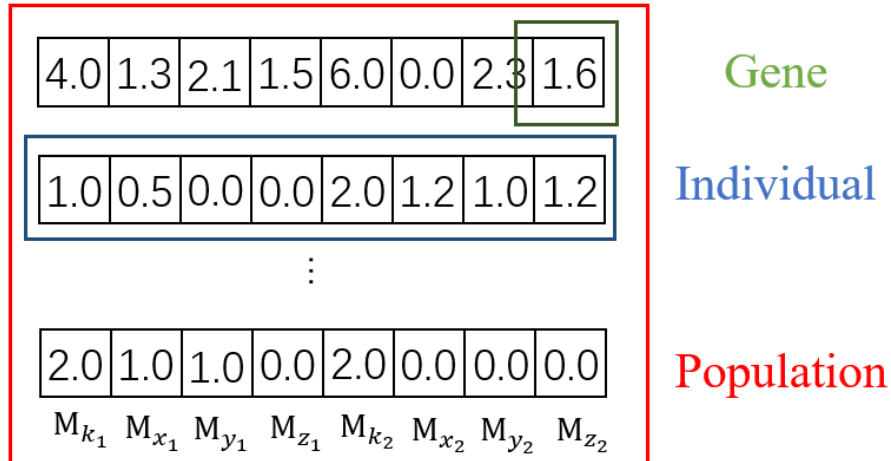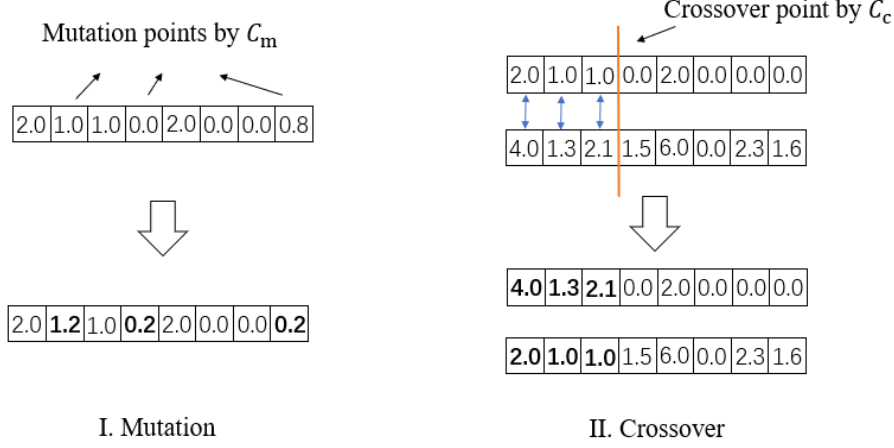

Figure 3: Population, individual and gene.

Figure 4: Mutation and Crossover.

Where $\boldsymbol{C} = \underbrace{[1, 1, \cdots 1]}_{m}$; $\boldsymbol{A} = \underbrace{[a_1, a_2, \cdots a_m]}_{m}^{T}$; $\boldsymbol{H}^T = \begin{vmatrix} Hx_1, & Hx_2, & \ldots & Hx_m \\ Hy_1, & Hy_2, & \ldots & Hy_m \\ Hz_1, & Hz_2, & \cdots & Hz_m \\ 1, & 1, & \ldots & 1 \end{vmatrix}$,

$\{Hx_m, Hy_m, Hz_m\}$ is the coordinate of points from the preprocessed hull $\boldsymbol{H}$; $\boldsymbol{N} = \begin{bmatrix} P_x, P_y, P_z, 1 \end{bmatrix}^T$, (P_x, P_y, P_z) is the coordinate of the studied point P.

If the point P is inside the studied point hull $\boldsymbol{H}$, there will be a solution A to Eq. 3, satisfying:

$$a_1 + a_2 + ... + a_m = 1, a_i > 0 \qquad (4)$$

Mutation and Crossover: Mutation and Crossover are strategies to produce offsprings. They are the most vital segments in GA and the key to finding the optimal solution.

Mutation refers to random change in the value of genes with a probability C_m, which stands for the change probability (Figure 4 I). This strategy is designed to control the exploration breadth and convergence rate. Crossover means the exchange of genes between two different individuals with a coefficient C_c, which determines the crossover point (Figure 4 II). This strategy is dedicated to filtering out better genes and promote positive diversity. A proper setting of C_m and C_c can maintain population diversity and prevent overfitting problems.

Evaluation: Evaluation involves the concept of fitness functions. It gives a fitness score, which determines the ability of this individual to compete with others in the population, to each individual. Here, the fitness function is defined as the following:

$$F(\boldsymbol{M}) = \sum_{i=1}^{m} (f_{H_i}^l(M) - 1)^2 \tag{5}$$

where $f_{H_i}^l(M) = \sum_{j=1}^{n} \frac{M_{k_j}}{\left(H_{x_i} - M_{x_j}\right)^2 + \left(H_{y_i} - M_{y_j}\right)^2 + \left(H_{z_i} - M_{z_j}\right)^2}$, H_i stands for a control point in the point hull $\boldsymbol{H}$.

Selection: Selection is based on the fitness score calculated in Evaluation. It is implemented to filter the fittest N individuals and pass them to the next generation. It is generally performed after mutation, crossover and evaluation. This makes individuals with higher fitness more likely to survive and reproduce.

2.2.2. Gradient Search for refinement of outer contour

In the refinement of outer contour by GS, two segments are included in GS: *Gradient Descent* and *the anomaly detection*. The flowchart of GS is detailed in Algorithm 2.

Algorithm 2 The Gradient Search for refinement of outer contour

---

Input: the preprocessed point hull H, the number of generations E^{gs}, the learning rate η, the Metaball model of the principal outer contour $\boldsymbol{M}^{ga}$.

Output: the metaball model for the refined outer contour $\boldsymbol{M}^{gs}$.

1: $\boldsymbol{M}^{ga}$ is taken as the inital parameter $\boldsymbol{M}_0$;
2: **for** $i = 1, 2, ...,$ to E^{gs} **do**   ▷ **1st Gradient Descent**
3:       $\boldsymbol{M}_0 \leftarrow \boldsymbol{M}_0 - \eta \cdot \nabla_{\boldsymbol{M}_0} L(\boldsymbol{M}_0)$;
4: **end for**
5: **Anomaly Detection -** Performing clearning on M_0 for two types of the anomaly points: control point overflow and sign abnormality. Sending the cleaned parameters M_1 into the next step;
6: **for** $i = 1, 2, ...,$ to E^{gs} **do**   ▷ **2nd Gradient Descent**
7:       $\boldsymbol{M}_1 \leftarrow \boldsymbol{M}_1 - \eta \cdot \nabla_{\boldsymbol{M}_1} L(\boldsymbol{M}_1)$;
8: **end for**
9: **Return:** The searched paramter set $\hat{\theta}$.

Gradient Descent: Gradient Descent is an optimization algorithm based on gradient information, which is readily available from the Metaball functions. For an objective function $L(M)$, its parameters can be updated iteratively to find the optimal:

$$M \leftarrow M - \eta \cdot \nabla_M L(M) \tag{6}$$

where M represents the parameters for Gradient Descent, here is the parameter set of the fitted Metaball model; η is the learning rate; $\nabla_M L(M)$ is the gradient of the $L(M)$ to the parameter M.

In this segment, the objective function for contour refinement is defined as a piecewise function instead of Eq. 2:

$$L(M) = \begin{cases} \sum_{i=1}^{m}(f_{H_i}^l(M) - 1)^2, & f_{H_i}^l \in [2, +\infty] \\ \sum_{i=1}^{m}|f_{H_i}^l(M) - 1|, & f_{H_i}^l \in [1, 2] \\ \sum_{i=1}^{m}\left[(f_{H_i}^l(M) - 1)^2 + \frac{1}{f_{H_i}^l(M)} - 1\right], & f_{H_i}^l \in [0, 1] \end{cases} \tag{7}$$

This is because many attempts have shown that a loss function in Mean Square Error(MSE) form can often result in distorted models with control points outside the targeted hull. This is related to the property of Metaball function. When the study point is internally close to or externally far from the Metaball hull, its corresponding function value will all be very small. This results in the value range of Eq. 2 as shown by lines in Figure 5, which makes the direct GS fall into the local optimal solution easily. This defect can be avoided through the implementation of Eq. 7. Under this form, the loss value of points outside and close to the Metaball hull can all be enlarged greatly (Dash lines in Figure 5). Such implementation can not only improve fitting efficiency but also adaptability to complex geometry of GS.

For gradient update, we adopt a pattern that the gradient for the whole dataset, the entire point hull H, will be calculated once for each round of iteration. This is because sufficient attention to all points on the targeted hull can endow the trained model with higher fidelity[39].

Anomaly Detection: Since the search of GS is strictly based on the gradient relationship, redundant control points can be merged reasonably in this process. But this also raises two other problems: control point overflow and sign abnormality. The control point overflow refers to solution with control points outside the target point hull H. And the sign abnormality
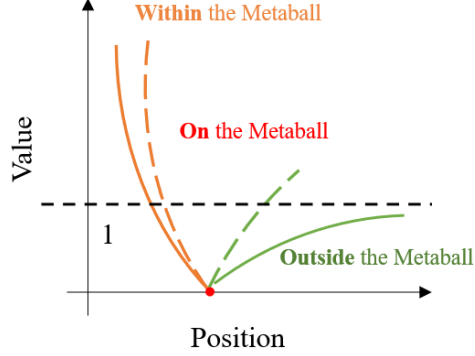
Figure 5: The objective function of MSE is depicted by the solid line in the graph, while the dashed line represents the loss function of Eq. 7. The later one increases the loss function value for points outside the point hull, improving the GS performance.

means solution with control points of negative k values. Those anomaly points will be cleared out by assigning a zero weight during this stage.

2.3. Micro-mechanical Models for Numerical Simulations with Metaballs

To probe the mechanical behavior of the avatar distilled by MI, DEM and LBM are implemented with Metaballs. The coupling takes a similar scheme as stated in [36?], thus only key points are included here for the sake of brevity.

2.3.1. Coupling with DEM model

DEM is a method tackling motions and effects of large number of individual particles[40, 41]. In this framework, the translation is expressed by Newton's equation while the rotation is described with the angular momentum conservation model:

$$
\begin{cases}
m_i \boldsymbol{a}_i = m_i \boldsymbol{g} + \sum_{j=1}^{N} \boldsymbol{F}_{ij}^c + \boldsymbol{F}_i^e \\
\frac{d}{dt} \left(\mathbf{I}_i \boldsymbol{\omega}_i \right) = \sum_{j=1}^{N} \boldsymbol{T}_{ij}^c + \boldsymbol{T}_i^e
\end{cases}
\tag{8}
$$

where m_i and $\boldsymbol{a_i}$ stand for the mass and acceleration of the i-th particle. $\boldsymbol{F}_i^e$ is the external force. $\boldsymbol{F}_{ij}$ means the contact force between the i-th particle and its neighbor particle j. I_i is the inertia tensor. ω_i is the angular velocity. T_{ij}^c and $\boldsymbol{T}_i^e$ represent torques caused by the external and contact force seperately. More details can be referenced in [36]

13

Here, the contact force F^c is described by the linear spring dashpot model[40]. The normal component of F^c is given by:$F_n^c = k_n \delta + \eta_n \left(v_j - v_i \right) \cdot n$, where k_n is the normal spring stiffness. δ is the particle overlapping distance. η_n is the normal damping coefficient. And n stands for the unit normal vector.

The tangential component of F^c is determined as:

$$\begin{cases} F_t^c & = \min \left(\mu_s F_n^c, F_{t0}^c \right) \\ F_{t0}^c & = \left\| -k_t \boldsymbol{\xi} - \eta_t \left(v_j - v_i \right) \cdot t \right\| \end{cases} \tag{9}$$

where μ_s stands for the static friction coefficient. k_t is the tangential spring stiffness. η_t refers to the damping coefficient. $\boldsymbol{\xi}$ is the tangential spring. And t is the unit tangential vector.

For DEM coupling, the collisions between Metaballs as well as Metaball and wall are handled properly. This requires three parameters: the contact point x_{cp}, the contact direction n and the overlap δ. To avoid unwanted intersection problems,the collision is first transformed to a sphero-Metaball based contact[36], where the original Metaball is approximated by a combination of zoomed internal Metaball and dilated sphere with radius R_s. Then, an optimization problem is introduced to locate the closest points on studied Metaball set or Metaball and wall. This optimization problem is defined as:

$$\begin{array}{ll} \text{Minimize} & f_0(\boldsymbol{x}) + f_1(\boldsymbol{x}) \\ \text{Subject to} & c_{tol} < \left| f_0(\boldsymbol{x}) \right| < 1, \quad c_{tol} < f_1(\boldsymbol{x}) < 1 \end{array} \tag{10}$$

where $f_0(\boldsymbol{x})$, $f_1(\boldsymbol{x})$ refer to functions of two Metaballs. c_{tol} stands for the tolerance to avoid $f_0(\boldsymbol{x}) + f_1(\boldsymbol{x}) = 0$ when $\|\boldsymbol{x}\| \to \infty$. Under this limitation, the distilled solution will make the gradient of Eq. 10 equal to 0:

$$\nabla(f_0(\boldsymbol{x}) + f_1(\boldsymbol{x})) = \boldsymbol{0} \tag{11}$$

On collisions between Metaballs, a Newton-Raphson method is used to search the local minimum point x_m. And the closest points on Metaballs (x_{c0} and x_{c1}) can be approximated by:

$$\begin{cases} \boldsymbol{x}_{c0} = \boldsymbol{x}_m + q_0 \nabla f_0(\boldsymbol{x}_m) \\ \boldsymbol{x}_{c1} = \boldsymbol{x}_m + q_1 \nabla f_1(\boldsymbol{x}_m) \end{cases} \tag{12}$$

14

By combining Taylor series expansion and $f_0(x_{c0}) = 1$, q_0 and q_1 can be expressed explicitly to calculate the x_{c0} and x_{c1}. Then, the required three parameters for collision between Metaballs can be defined as:

$$\begin{cases} \boldsymbol{x}_{cp} = \boldsymbol{x}_{c0} + (R_{s0} - 0.5\delta)\boldsymbol{n} \\ \boldsymbol{n} = \frac{\boldsymbol{x}_{c0} - \boldsymbol{x}_{c1}}{\|\boldsymbol{x}_{c0} - \boldsymbol{x}_{c1}\|} \\ \delta = R_{s0} + R_{s1} - \|\boldsymbol{x}_{c1} - \boldsymbol{x}_{c0}\| \end{cases} \tag{13}$$

On collisions between Metaball and wall, the problem is simplified into finding a point x_{cw}^W on the wall with normalized gradient of $(-1, 0, 0)$ to rotated Metaball function. This point is searched similarly by a Newton-Raphson method. Then the closest point on Metaball to wall is defined as:

$$\boldsymbol{x}_{cp}^W = \boldsymbol{x}_{cw}^W + q^W \nabla f^W(\boldsymbol{x}_{cw}^W) \tag{14}$$

With $f^W(\boldsymbol{x}_{cw}^W) = 1$ and Taylor series expansion, the required three parameters for collision between Metaball and wall can be defined as:

$$\begin{cases} \boldsymbol{x}_{cp} = \boldsymbol{x}_{cw} + 0.5\delta\boldsymbol{n} \\ \boldsymbol{n} = \frac{\boldsymbol{x}_{cm} - \boldsymbol{x}_{cw}}{\|\boldsymbol{x}_{cm} - \boldsymbol{x}_{cw}\|} \\ \delta = R_s - \|\boldsymbol{x}_{cm} - \boldsymbol{x}_{cw}\| \end{cases} \tag{15}$$

2.3.2. Coupling with LBM model

LBM is a popular Computational Fluid Dynamics scheme based on kinetic theory. Instead of solving flows at the continuum scale, the Boltzmann equation is used to describe fluid motions, in which the distribution functions are the basic variable. The distribution function $D_i(\boldsymbol{x}, t)$ representing the probability that a molecule of fluid occupies a cell at position $\boldsymbol{x}$ with a given discrete velocity $\boldsymbol{e_i}$ at time t. More details on how Navier-Stokes equations can be solved by LBM can be found in [21].

For DEM-LBM coupling, the boundary condition, hydrodynamic force and refilling algorithm are selected carefully. On moving boundary condition, the interpolated bounce-back (IBB)[42] is deployed to capture the influence of Metaball particles on the fluid and impose the non-slipping boundary condition. This scheme divides the involved nodes into fluid nodes, solid nodes and boundary nodes (fluid nodes that are next to the solid boundary)[?]. These nodes are symbolized with "s" - the closest solid node, "w" - the wall, "f" - the boundary node, and "ff" for the neighbouring fluid node of

"f" as shown in Figure 6. Under this definition, the distribution function of a point which departs from x_d with velocity $e_{i'}$ (i' is the direction opposite to i), hits on the wall and returns back to x_f with velocity e_i is defined as:

$$D_i(\boldsymbol{x}_f, t + \Delta t_{LBM}) = D_{i'}^+(\boldsymbol{x}_d, t) + 6\omega_{i'}\rho_f \frac{\boldsymbol{e}_i \cdot \boldsymbol{u}_w}{C^2}, \tag{16}$$

where ω_i are the LBM weights for each discrete direction; ρ_f represents the fluid density; the particle surface velocity $\boldsymbol{u}_w = \boldsymbol{v}_{pj} + \boldsymbol{w}_{pj} \times (\boldsymbol{x}_w - \boldsymbol{x}_{pj})$, where $\boldsymbol{v}_{pj}$ and $\boldsymbol{w}_{pj}$ are the translational and angular velocity at the jth particle's centroid $\boldsymbol{x}_{pj}$, respectively. $D_{i'}^+(\boldsymbol{x}_d, t)$ is the post-collision distribution function and can be decomposed into equilibrium and non-equilibrium parts:

$$D_{i'}^+(\boldsymbol{x}_d, t) = D_{i'}^{eq}(\rho_d, \boldsymbol{u}_d) + D_{i'}^{neq}(\boldsymbol{x}_d, t), \tag{17}$$

The $\boldsymbol{u}_d$ in above equation can be expressed explicitly by linear interpolation:

$$\boldsymbol{u}_d = \frac{1}{3}\boldsymbol{u}_d^* + \frac{2}{3}\boldsymbol{u}_d^{**}. \tag{18}$$

where $\boldsymbol{u}_d^* = \begin{cases} 2q\boldsymbol{u}_f + (1-2q)\boldsymbol{u}_{ff}, & q \leqslant 0.5, \\ \\ \frac{1-q}{q}\boldsymbol{u}_f + \frac{2q-1}{q}\boldsymbol{u}_w, & q > 0.5, \end{cases}$, q can be obtained by solving $f(\boldsymbol{x}_f + q\boldsymbol{e}_i) = c_0$, and c_0 is a Metaball function value depending on R_s; $\boldsymbol{u}_d^{**} = \frac{1-q}{1+q}\boldsymbol{u}_{ff} + \frac{2q}{1+q}\boldsymbol{u}_w$. More details on this IBB scheme can be found in [**?**].

On hydrodynamic forces, a momentum exchange method (MEM)[43] is utilized. MEM is a frequently used scheme for fluid-particle interactions, where the hydrodynamic force is defined as the sum of the momentum exchanges among all discrete velocity colliding with solid surfaces. To obey the Galilean invariance principle, a Galilean-invariance MEM[44], which can efficiently avoid numerical noises, is implemented.

As a DEM particles vacates LBM cells, some missing D_i comming out of the particle must be initialized. To achieve this, a local refilling algorithm based on bounce-back rule is applied. The reinitialized distribution function is defined as:

$$D_i(\boldsymbol{x}_{new}, t) = D_{i'}(\boldsymbol{x}_{new}, t) + 6\omega_{i'}\rho_f \frac{\boldsymbol{e}_i \cdot \boldsymbol{u}_w}{C^2}, \tag{19}$$

where $\boldsymbol{x}_{new}$ is the new fluid node position. If $D_{i'}(\boldsymbol{x}_{new}, t)$ does not exist, the equilibrium refilling is used: $D_i(\boldsymbol{x}_{new}, t) = D^{eq}(\rho_0, \boldsymbol{u}_{new})$, where $\boldsymbol{u}_{new} = \boldsymbol{v}_{pj} + \boldsymbol{w}_{pj} \times (\boldsymbol{x}_{new} - \boldsymbol{x}_{pj})$.
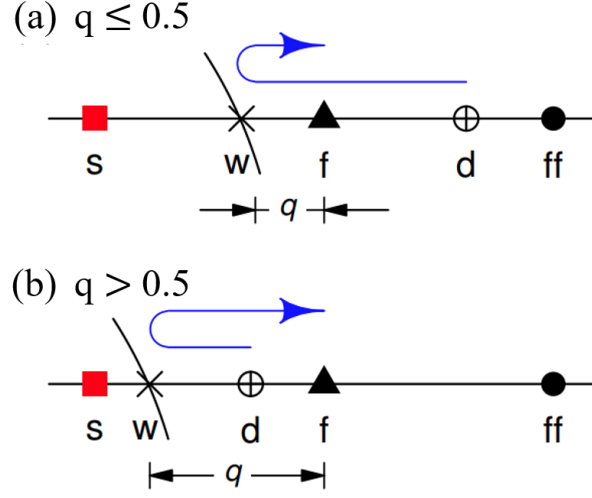
Figure 6: The schematic of interpolated bounce-back rule for different q. The red square, symbolized with "s", stands for the closest solid node. The cross, symbolized with "w", represents the wall. The triangle, symbolized with "f", means the boundary node. The circle, symbolized with "ff", stands for the neighbouring fluid node of "f". And the hollow circle with cross, symbolized with "d", represents the depart position.

3. Validations

To validate the proposed algorithm, we conducted simulations on Jeffery Orbits[45] of ellipsoidal particles and settling of irregular-shaped particles in viscous fluid. Comparisons are made on important indicators of these physical processes.

3.1. Jeffery Orbits of Ellipsoidal Particles

The motion of rigid ellipsoidal particles in shear flows is analyzed theoretically by Jeffery[45]. A rigorous analytical solution of the rotary motion of particles is given, where the periodic motion of particles is named as Jeffery orbits[46, 47, 48]. For an isolated, neutrally buoyant ellipsoidal particle located at origin in a field of laminar fluid described as:

$$
\begin{aligned}
U_x &= \dot{\gamma} z \\
U_y &= 0 \\
U_z &= 0
\end{aligned}
\tag{20}
$$

17

U_x, U_y and U_z are the fluid velocities along axes, $\dot{\gamma}$ the shear rate of flow field, its Jeffery orbit can be characterized with the following rotation period:

$$T = \frac{2\pi \left(a^2 + b^2\right)}{ab\dot{\gamma}} \tag{21}$$

where a and b are major and minor axes separately.

To evaluate the ability of MI-DELBM to capture the rotation of particles, we make a comparison between the theoretical and simulated results on the Jeffery orbit. The simulation setup and an example snapshot are shown in Figure 7. We simulate the motion of ellipsoidal particles in various viscous shear flows within a 3D channel. The dimension of this channel is set to be: $0.15 \times 0.15 \times 0.15 m$. The involved particles are represented uniformly with Metaball models of 10 control points as shown in Table 1. The aspect ratio AR of them ranges from 1.0 to 5.0 by varying the major axis. To avoid the negative impact of the distance between walls on the period result[49, 50, 46], the minor axis of particle is chosen to be $0.01m$. These particles are located at the center of this channel with major axis in the xz plane. The fluid density and viscosity are $940.0 kg/m^3$ and $0.5\ Pa \cdot s$. Linear shears with shear rate of 1.0, 1.5 and 2.0 are introduced to the flow, by applying moving boundaries on the top and bottom plates. The particle density is also chosen to be $940.0 kg/m^3$, avoiding the effect of buoyancy[46, 47]. The LBM and DEM time steps are both set to be $2.0 \times 10^{-4} s$, since no particle contact is involved. The LBM space step is set to be $1.0 \times 10^{-3} s$.

Figure 8 illustrates the result of the above simulations. A good match can be found between the theory and simulation. With the advantage of representing realistic ellipsoidal particles, MI-DELBM achieves better agreement than the published work[51]. Note that small deviations can be observed in some cases, which possess large aspect ratios of particles and shear rates of fluid. This is mainly caused by the high Renold number $Re\ (> 2)$, since the Jeffery model applies for particle motion at vanishing Re[45, 52]. Here, Re is defined as:

$$Re = \frac{\rho_f U_f a}{\mu} \tag{22}$$

where ρ_f means the density of fluid. U_f represents the fluid velocity. And μ represents the viscosity of the fluid. Besides, as the increase of aspect ratios, the edges of ellipsoidal particles get closer to the boundaries, contributing to the deviation [50, 46].

Table 1: The involved ellipsoidal particles for validations on the Jeffery orbit. The meshes are only for visualization. All particles are represented with Metaball models in simulations.

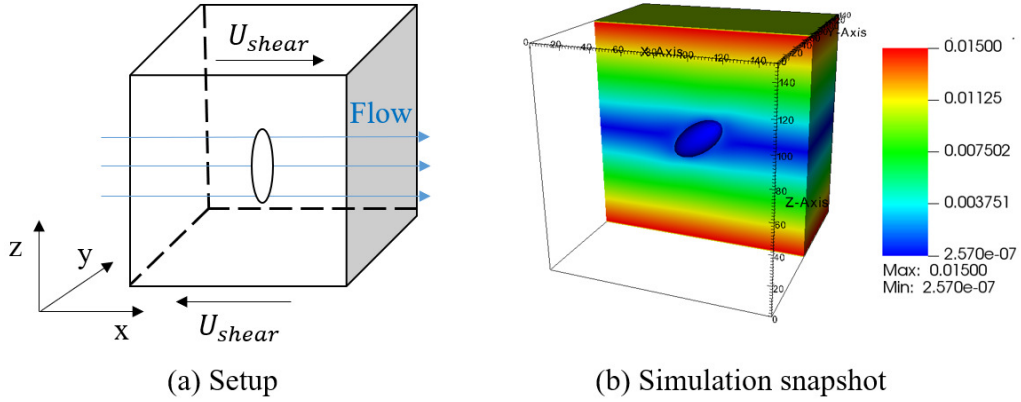| Aspect Ratio	1	2	3	4	5
Particle Mesh					

(a) Setup

(b) Simulation snapshot

Figure 7: The setup and snapshot of simulations on the Jeffery orbit. The color in the background stands for the fluid velocity. The distance in simulations is made dimensionless by dividing 0.001. And the actual dimension of domain is: $0.15 \times 0.15 \times 0.15m$. The U_{shear} stands for the shear velocity.
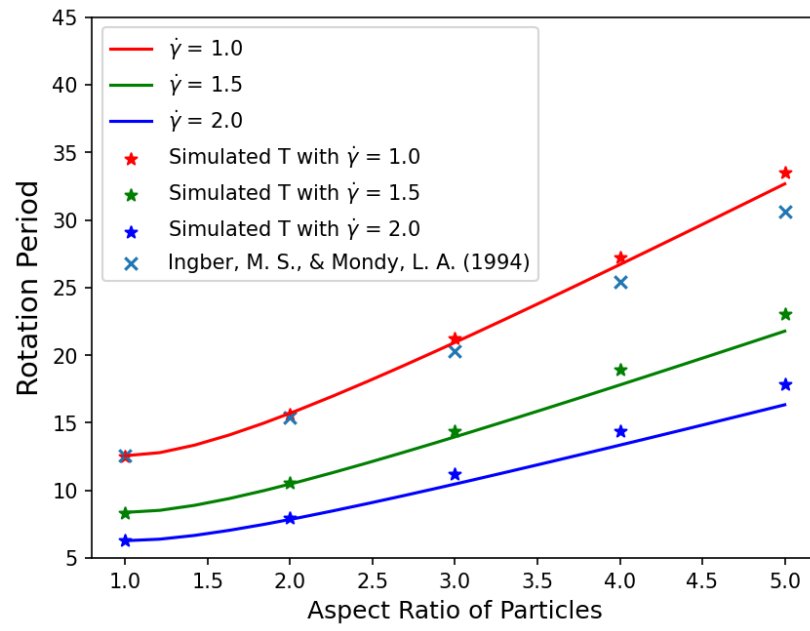
Figure 8: The rotation periods of ellipsoidal particles with different aspect ratios in fluids of various shear rates.
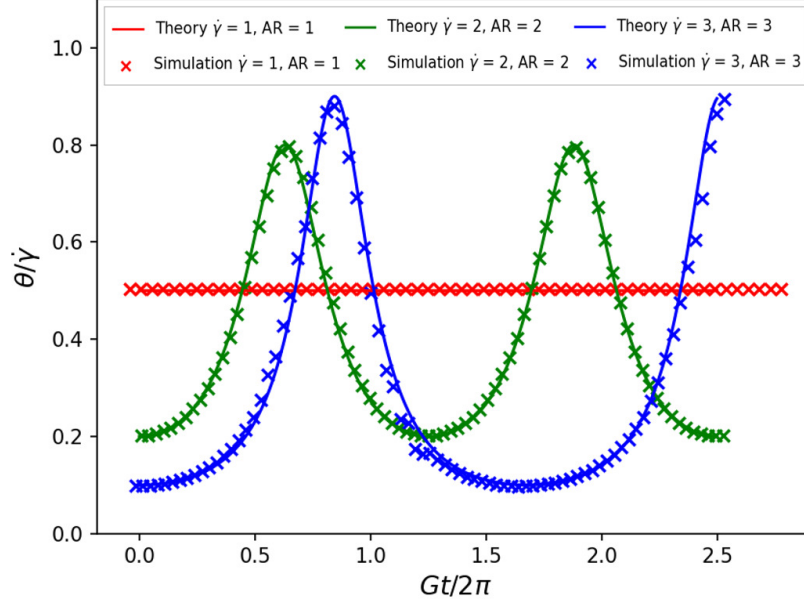
Figure 9: A comparison on the spanwise component of the angular velocity of three cases at low Re between the analytical solution and simulated result of the Jeffery orbit.

As further validations, we also evaluate the spanwise component of the angular velocity on three cases at low Re. As shown in Figure 9, an excellent agreement can be found with the following theoretical solution:

$$\dot{\theta} = \frac{\dot{\gamma}}{a^2 + b^2} \left(a^2 \cos^2 \theta + b^2 \sin^2 \theta \right) \tag{23}$$

where θ is the spanwise component of the particle rotation angle.

3.2. Particle Settling in Viscous fluid

As the basic of many complex physical processes, the gravity-driven settling of particles has attracted considerable attentions[53, 54]. Recently, progress has been made on sedimentation of non-spherical particles. For example, Ardekani et al. analyze the settling of ellipsoidal particles with Immersed Boundary Method[52]. A.Xu et al. investigate the thermal effects on the settling of elliptical particles through the double-distribution multiple-relaxation-time lattice Boltzmann[55]. Rishabh More et al. explore the effect of shape anisotropy on the sedimentation of particles in density

21
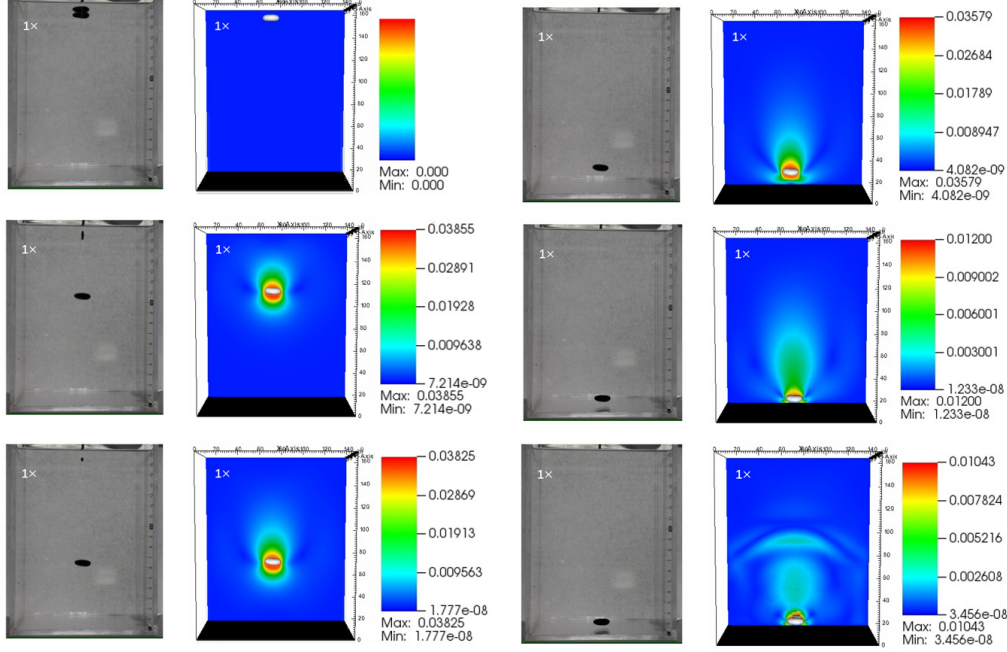
Figure 10: The experiment and simulation snapshots of irregular-shaped cobblestone-settling in viscous fluid. The color stands for the fluid velocity.

stratified fluid[56]. Changjiang Zhou et al. report a study on the settling of disc-shaped particles with imaging experiments[57]. However, few attempts have been made with morphologies of realistic particles. This creates opportunities for the application of MI-DELBM but also makes it hard to evaluate its accuracy on realistic particles.

To further evaluate the ability of MI-DELBM to characterize the translation and rotation of particles, we thus make validations on the settling of avatars distilled from XRCT images taken on three different irregular-shaped natural cobblestones in viscous fluids with experiments. The setup is shown in Figure 10 as well as simulation snapshots for one to one comparison. The experiments are carried out in a rectangular container with outside dimension: $0.15 \times 0.15 \times 0.20m$ and internal dimension: $0.14 \times 0.14 \times 0.195m$.

The shapes of these cobblestones are shown in Figure 11 (a), which are irregular and different. The densities and volumes are $2850.67kg/m^3$ and $6.314 \times 10^{-7}m^3$ for cobble A, $2559.838kg/m^3$ and $9.063 \times 10^{-7}m^3$ for cobble B as well as $2957.951kg/m^3$ and $6.119 \times 10^{-7}m^3$ for cobble C. Three types of
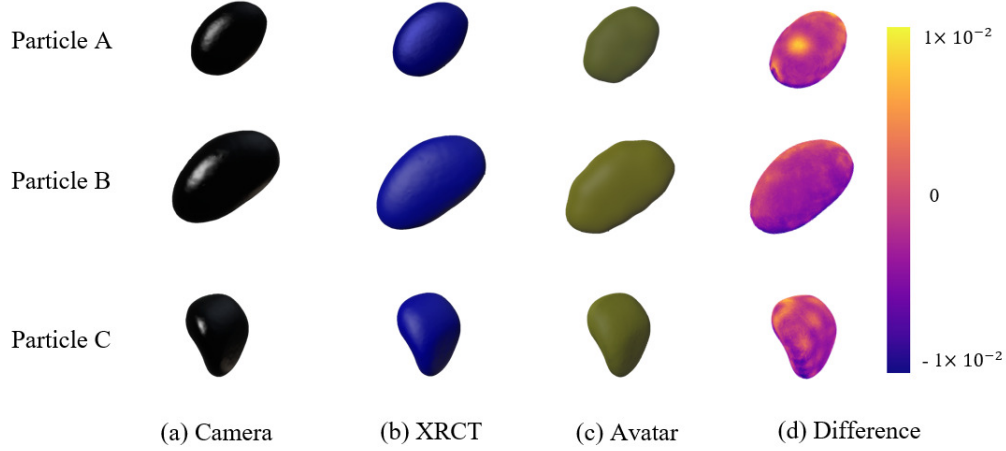
Figure 11: Visualization of the experimental cobblestones (a) High-speed camera images (b) XRCT images (c) The Metaball avatar (d) Difference between XRCT and avatar - the color stands for the loss value of each hull point from XRCT on the Metaball avatar in Eq. 7, the average loss values of these particles are 6.1×10^{-3} - particle A, 4.1×10^{-3} - particle B and 3.8×10^{-3} - particle C.

dimethyl silicone oil with viscosity 0.088, 0.295 and 0.853 $Pa \cdot s$ are used as the viscous fluid in experiments(Measured by LICHEN NDJ viscometer). The cobblestones are released by tweezers in a completely submerged state. The initial release orientation is set to make the maximum projection plane as perpendicular to the settling direction as possible. The setting trajectory of cobblestones are recorded by a high-speed camera (CANON EOS 5D MARK IV). The settling velocity is extracted with MATLAB by the pixel change of cobblestone centroid between video frames.

The XRCT image, for shape digitization, is captured with a ZEISS Xradia 610 Versa. The voxel size is $45.476311 \mu m$ and optical magnification 0.395810. The particle in the simulation contains 7.974538×10^6 voxels in average to represent the real geometry. The particle segmentation is done by "ilastik"[58], an edge detection algorithm for segmentation of XRCT images aided by machine learning. Different from function methods, "ilastik" detects particle edges by considering both voxel intensity and brightness gradient. This avoids omitting particles with concave spots on the surface or broken spots on the edge[59]. The segmented particles are shown in Figure 11, (b).

To make one to one comparisons, the settings of simulations are identical

23

to the experiments. Furthermore, no parameters are calibrated in the simulation since the MI-DELBM is a fully solved scheme, the only free parameter is the fluid viscosity which is measured independently. The MI avatars are produced with the following hyperparameter settings: $E^{ga} = 100$, $N_I = 1200$, $N_G = 100$, $C_m = 0.6$, $C_c = 0.5$, $E^{gs} = 100000$ and $\eta = 0.001$, the shapes of these cobblestones are captured by the MI algorithm as avatars shown in Figure 11 (c). Comparisons (Figure 11 d) indicate MI to be a reliable tool to capture particle morphology. It is worth noting that the surface mesh is only for visualization and those particles are presented as Metaballs in the simulation system. The LBM and DEM time steps are set as: 2.0×10^{-4} and $2.0 \times 10^{-6} s$. The LBM space step is set as $1 \times 10^{-3} m$. In the following discussion, Re is defined as:

$$Re = \frac{\rho_f U_p D_e}{\mu} \tag{24}$$

where U_p is the peak velocity of the particle. D_e stands for the diameter of the equal-volume sphere.

Overall, the simulation results match well with the experiments for all Re considered. Figure 12, 13 and 14 show the vertical-velocity time series for particle A, B and C in both experiments and simulations respectively. For particle A, a little rotations are observed in the experiments which were not observed in the simulations. This could be caused by the fact that the initial releasing orientation of particle cannot be controlled strictly by hand due to complexity of realistic morphologies. Such discrepancy will not interfere the settling velocity, since the shape representation with Metaballs is accurate. But small deviation will be introduced to the comparison depending on the shape complexity of particles. For particle B, small deviations can be observed in the initial stage at $Re = 1.48$ and 6.87. This is also related to the imperfect releasing orientation. With more complex shape, particle B needs more time to adjust itself at the initial stage to maximize its projection area and this results in observed deviations. For particle C, many rotations are observed in experiments, especially at $Re = 36.46$. Regarding geometry, particle C has the most complex shape, which makes its initial release orientation hard to satisfy for the perpendicular condition. This explains the small deviations in the initial stage for particle C at $Re = 1.30$ and 7.07. As for $Re = 36.46$, the relatively high Re makes the particle vulnerable to disturbance. This leads to a more intense rotation for orientation adjustment in the ultimate stage, which causes the curve fluctuation. However, the error
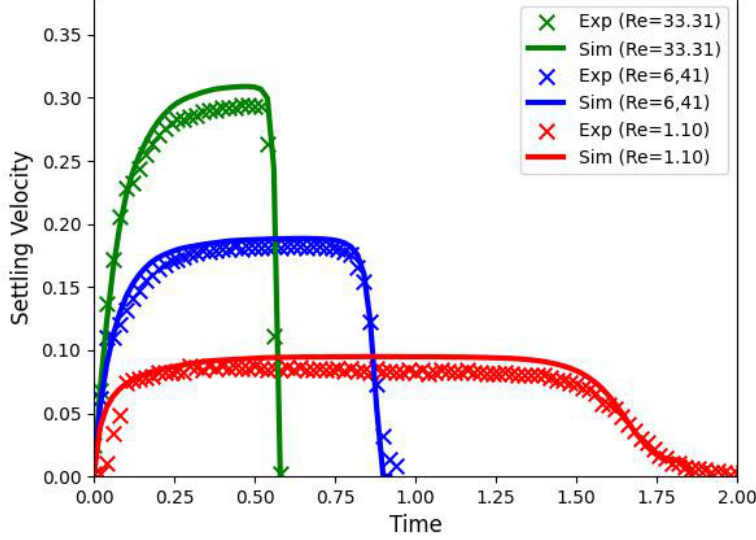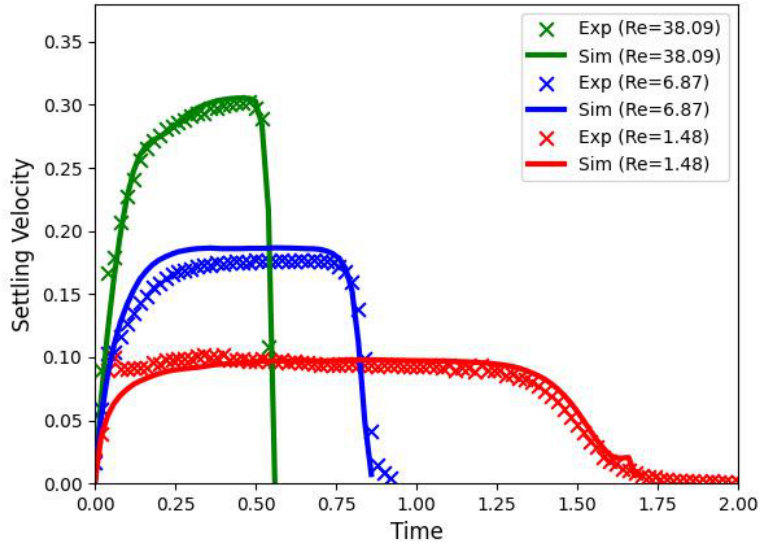
24

Figure 12: The comparison of vertical velocity between the simulation and experiment for Particle A during the settling.

of the steady settling velocity is all within an acceptable range, which further proves the robustness of the proposed method.

4. Computational Efficiency

To investigate the efficiency of MI-DELBM, we carry out a comparison with the sphere-based framework. Since the cost of simulating a fluid-particle system focuses on the fluid part[21, 6], we implement the same type of LBM in both frameworks. Considering the variety of sphere-clustering methods[15, 16, 60], it is hard to make comparisons on irregular-shaped particles. Thus, the settling of spheres of different numbers in viscous fluid is selected for simulations (Figure 15). The settlings are carried out in a domain with size: $0.15 \times 0.15 \times 0.15 m$. The number of spheres ranges from 1 to 350. These particles are located at the top part ($> 0.11m$) of domain randomly. The density of fluid and particles are $940.0 \ kg/m^3$ and $2940 \ kg/m^3$. The viscosity of fluid is set to be $0.088 \ Pa \cdot s$. The LBM and DEM time steps are set as: 2.0×10^{-4} and $2.0 \times 10^{-6} s$. The total steps of both LBM and DEM are 25,000. The LBM space step is set as $1 \times 10^{-3} m$. All simulations are run

Figure 13: The comparison of vertical velocity between the simulation and experiment for Particle B during the settling.
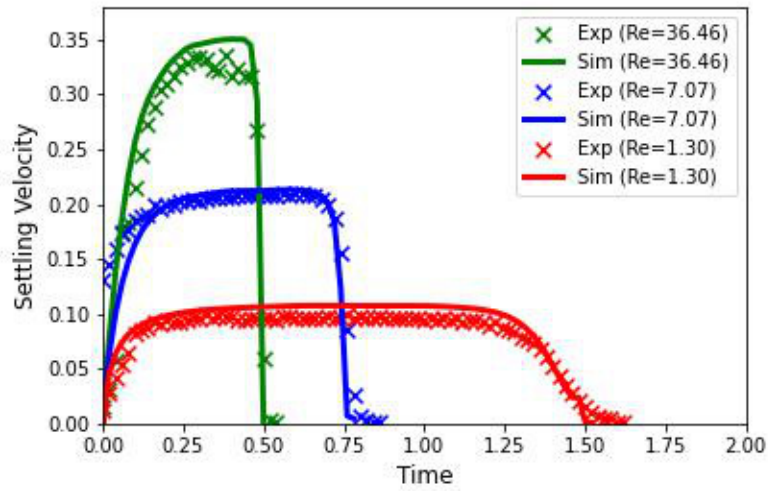

Figure 14: The comparison of vertical velocity between the simulation and experiment for Particle C during the settling.
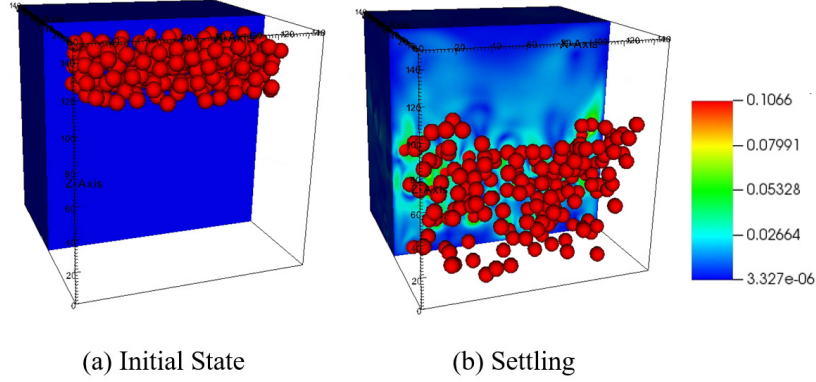
(a) Initial State   (b) Settling

Figure 15: Simulation snapshots of the sphere settling for efficiency evaluation. The red spheres are the settling particles, which are represented with the Metaball and sphere model in different attempts. The background color depicts the fluid velocity.

on a workstation with Intel Xeon W-2133 processor in parallel mode with OpenMP.

Figure 16 illustrates the time cost of MI-DELBM and sphere-based LBM frameworks. It can be observed that the time efficiency of the above two methods is very close on a small amount (< 100) of particles. As the increase of particle number, the cost of MI-DELBM gradually exceeds that of sphere-based methods. While the overall time costs of these two methods are within the same order of magnitude. Despite this, MI-DELBM can be more efficient in simulating realistic particles than sphere-based LBM framework due to the advantage of the Metaball function in representing complex morphologies. To accurately represent irregular-shaped particles without obvious artificial surface roughness, sphere-based techniques usually require clustering of thousands of prime spheres, which each requires 4 parameters for shape representation (position $\hat{x}_i$, $\hat{y}_i$, $\hat{z}_i$ and the radius)[14, 15, 16]. Similarly, the prime component of Metaballs, the control point, also need 4 parameters(position $\hat{x}_i$, $\hat{y}_i$, $\hat{z}_i$ and its coefficient $\hat{k}_i$) for shape characterization. However, tests and trails reveal that a relatively small number of control points (in the dozens for common particles such as cobblestones and Ottawa sands, and around 100 for more complex angular and concave sands) are sufficient for the Metaball model to accurately represent these shapes. This makes the coupling of Metaballs with micro-mechanical models much cheaper than that of the clusterd spheres. Overall, these results support the
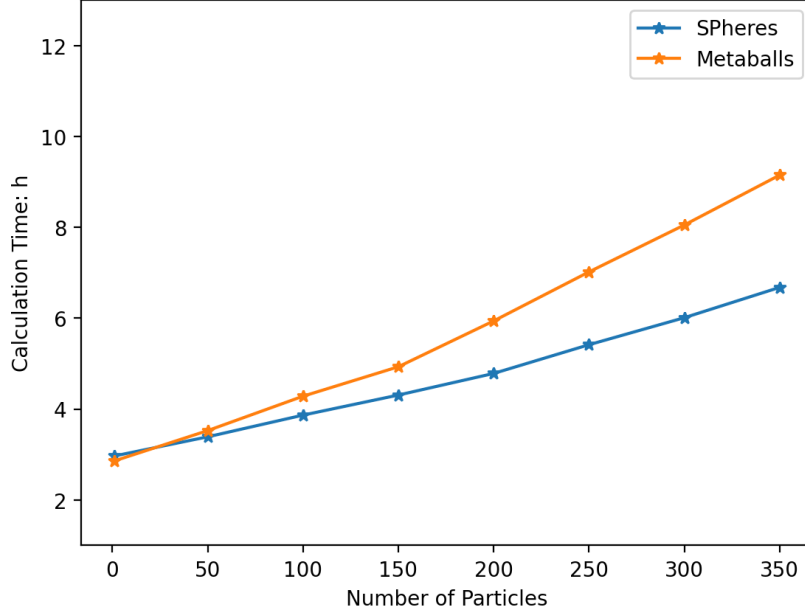
27

Figure 16: Time costs of settlings of various numbers of spheres in viscous fluid with MI-DELBM and sphere-based LBM

efficiency of MI-DELBM. The LBM and DEM time steps are both set to be $2.0\times10^{-4}s$ and . The LBM space step is set to be $1.0\times10^{-3}s$.

5. Application Showcases

Particle shapes can have significant influences on behaviors of fluid-particle systems[6, 61, 62]. MI-DELBM provides us with an efficient and powerful method to study the impact of morphological parameters on physical processes. To demonstrate its capability, here we conduct two simple application showcases on problems involving fluid-particle systems with complex-shaped particles.

5.1. The Drag and Lift Forces for realistic Particles

The fluid dynamic forces (e.g. the drag and lift forces) are important in particle-laden flows due to their correlations with bulk behaviors, such the agglomeration, sedimentation and diffusion [63, 64]. During the past decades, attempts have been made on modelling these forces acting on irregular-shaped particles. Among them, the direct numerical simulation method is a

28

popular one, because of the size distribution and shape diversity of irregular-shaped particles[65, 66, 67]. A good example is that M. Sommerfeld and Z. Qadir explores the drag and lift forces of irregular convex-shaped particles with LBM[68]. Another interesting study is Giorgia Tagliavini et al. develop a drag correlation for spheroids, where the influences of particle incident and aspect ratio are investigated in detailed[69]. However, the drag and lift forces of realistic particles are not yet fully studied yet.

Thus, we select two realistic particles, a cobblestone and an Ottawa sand, and image them with Metaballs (Figure 17 a). They have almost the same circularity C (= 0.98), which evaluates the roundness of non-spherical particle[70]:

$$C = \frac{\pi d_s}{P_p} \tag{25}$$

where P_p is the the perimeter of the particle's projected-area. And the d_s takes the following form[6]:

$$d_s = \sqrt{\frac{4A_p}{\pi}} \tag{26}$$

where A_p represents the maximum projected area of the particle. The simulation setup is shown in Figure 17 (b). The domain is set to have a constant inflow velocity $U_{in}(0.05 \ m/s)$ and a gradient free outlet with size: $0.15 \times 0.15 \times 0.15m$. Periodic boundary conditions are applied to rests. The fluid density is 1000 kg/m^3. The disturbance of flow is controlled with Re by varying the viscosity. In simulation, three states of Re (= 1, 10 and 50) are implemented. The volume of particles are chosen to be equal to the sphere with radius of $0.005m$, avoiding the domain size effect on the result of drag and lift forces[69]. The LBM and DEM time steps are both set to be $2.0 \times 10^{-4}s$. The LBM space step is set to be $1.0 \times 10^{-3}s$. Here, Re is redefined as:

$$Re = \frac{\rho_f U_f D_e}{\mu} \tag{27}$$

To include the impact of particle orientation to the inflow direction, multiple simulations are conducted, where the particles are rotated in steps of 40° around the x and y axis respectively. In each simulation, the forces are averaged over the 500 time steps after the flow is stabilized. For evaluation, the coefficients of the drag and lift forces are calculated and compared. The drag force is calculated with the simulated hydrodynamic force F_D along the

29

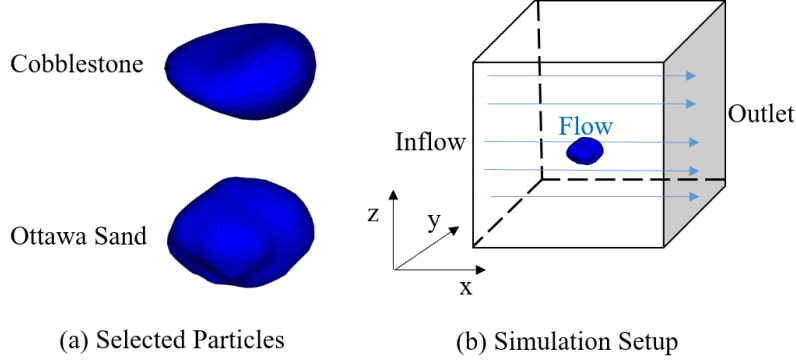(a) Selected Particles   (b) Simulation Setup

Figure 17: The selected realistic particles and simulation setup for the evaluation of drag and lift forces.

flow direction:

$$C_D = \frac{F_D}{\frac{\rho_f}{2} U_{in}^2 A_{eq}} \tag{28}$$

where A_{eq} is the cross section area of the volume equivalent sphere, of which the radius is $0.005m$.

And the lift force is determined with the simulated hydrodynamic force F_L perpendicular to the flow direction:

$$C_L = \frac{F_L}{\frac{\rho_f}{2} U_{in}^2 A_{eq}} \tag{29}$$

Figure 18 illustrates the typical result of flow fields around the selected two realistic particles with $Re = 1$ and 50. In the case of low Re, the flow wraps the particles closely. And as the increase of Re, the flow starts to separate and forms an obvious wake. A similar phenomena is observed on irregular-shaped, convex particles in [68].

The orientation-averaged drag and lift coefficients are shown in Figure 19 to 20. All indexes decrease with the increase of Re and tend to be stable. This is because the flow is attached to particles at low Re, resulting in relatively large coefficients. As the increase of Re, the separation of flow gradually enhances, yielding lower coefficients. Note that although the shapes of selected particles are different, the mean C_D of these two particles almost collapse. A similar result is reported in [68], where several particles with the same sphericity produced very close mean values of C_D. Besides, The rest indexes
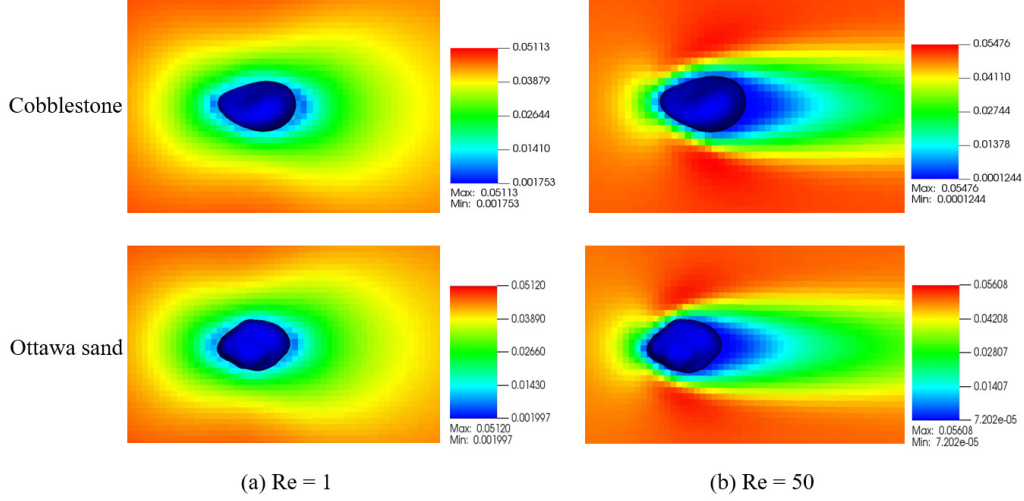
Figure 18: The selected realistic particles and simulation setup for the evaluation of drag and lift forces. The colors in background stands for the flow velocity field.

(the mean C_L, the standard deviation of C_D and C_F) are different but all in parallel modes. The above phenomena together indicate that comparisons based on single shape factor cannot fully illustrate the systematic impact of morphologies on the drag and lift coefficients.

5.2. The "Drafting, Kisssing, and Tumbling" (DKT) Phenomenon of Pair Particles with non-spherical morphologies

It is well known that settling of pair spheres follows the "drafting, kissing and tumbling" (DKT) process[71]: the following particle will surpass the leading particle due to the drag reduction from the wake of the leading particle. In recent years, advances have been achieved in the impact of particle shapes on the DKT process. For example, Ardekani et al. examine the pair interaction during settling with spheroids[52]. Shengli Ma et al. introduce sand-like particles to analyse more complex morphologies[72]. Kaituo Jiao et al. evaluate the influence of polygenal shapes in now-newtonian fluids[73]. However, how a more complex, realistic particle shape affects the DKT process is not fully explored quantitatively.

Therefore, we carry out a series of DKT simulations with multiple non-spherical particles, including non-convex and realistic ones (Cobblestone like) to thow the potential of MI-DELBM on this topic. All involved particles are
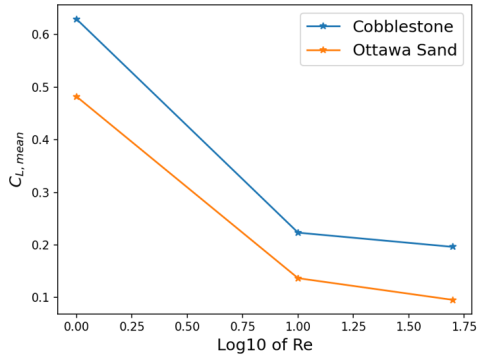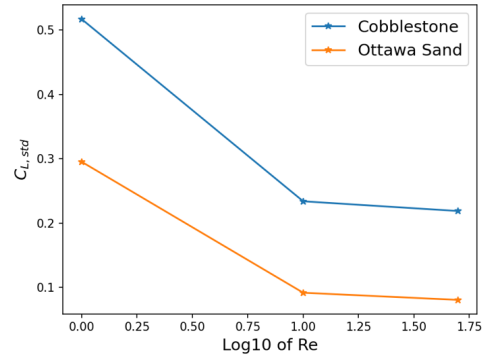
31
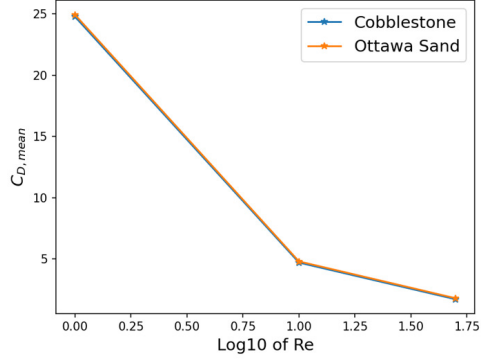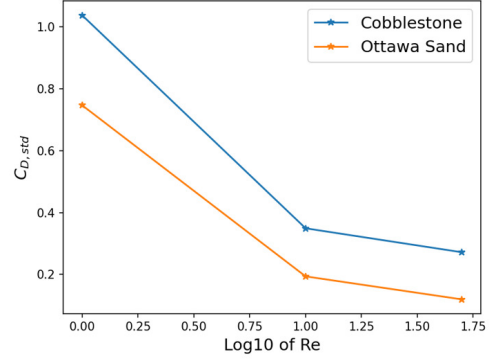
(a) The mean value

(b) The standard deviation

Figure 19: The drag coefficients of selected particles at different Re

(a) The mean value

(b) The standard deviation

Figure 20: The lift coefficients of selected particles at different Re

set with the same density 2800 kg/m^3 and volume 1e-6 m^3. Simulations are carried out in a rectangular container with dimension: $0.20{\times}0.20{\times}0.30m$ (W=0.20m, H=0.30m). The fluid density and viscosity are 976 kg/m^3 and 0.104 m^2/s. The pair particles are placed at 0.270 and 0.255 m from bottom initially, with a horizontal distance of 0.004 m. To study the impact of shapes quantitatively, four morphological parameters are introduced, namely, the sphericity (Φ), nominal diameter (d_n), surface-equivalent-sphere diameter (d_s), and Corey Shape Factor (CSF).

The sphericity (Φ) [6]is a frequently used shape factor for non-spherical particles and is defined as:

$$\Phi = \frac{S_{\text{sphere}}}{S} \tag{30}$$

where S_{sphere} represents the surface area of the volume-equivalent sphere to the studied particle. S stands for the surface area of the studied particle.

Another two widely used parameters are nominal diameter d_n[6] and surface-equivalent-sphere diameter d_s. The d_n is defined as the diameter of the volume-equivalent sphere. And the d_s is already listed in Eq. 26.

The CSF[74] reveals the dimension feature of the studied particle, as given by

$$CSF = \frac{d_s}{\sqrt{d_i d_l}} \tag{31}$$

Since limited particles can be obtained from XRCT due to cost problems, the involved particles, P_1 to P_8, are designed manually to have stepped morphological parameters, of which CSF is the main varying parameter (Table 2). A lower CSF means higher degree of difference. In visualization, control points of these particles are moved away gradually (Figure 21).It is worth noting that $P1$ is the volume equivalent sphere to the rest of the involved particles. The diameter of $P1$ is $D_e = 0.0125\ m$. We also select a cobblestone particle, T_9, which has the same shape features of P_8 except the sphericity. The MI avatar of it is shown in Figure 21. It can be observed that the difference in sphercity brings higher degree of anisotropy into T_9, compared to P_8.

The results show that non-spherical particle motions follow similar patterns as spheres. It also suggests that morphological parameters play an important role in DKT process. Henceforth, the vertical position is normalized by H, time by $t_r = \sqrt{H/g}$, velocity by $\sqrt{Hg}$, angular velocity by $2\pi/t_r$ and distance between particles by D_e.

33

Table 2: The morphological parameters of the particles in DKT

Particle	Sphericity	dn/ds	CSF
P1	1.0000	1.0000	1.0000
P2	1.0000	0.9845	0.9563
P3	0.9937	0.9718	0.9173
P4	0.9812	0.9514	0.8535
P5	0.9633	0.9335	0.8002
P6	0.9440	0.9172	0.7521
P7	0.9225	0.8959	0.7075
P8	0.8966	0.8780	0.6648
T9	0.9460	0.8738	0.6663
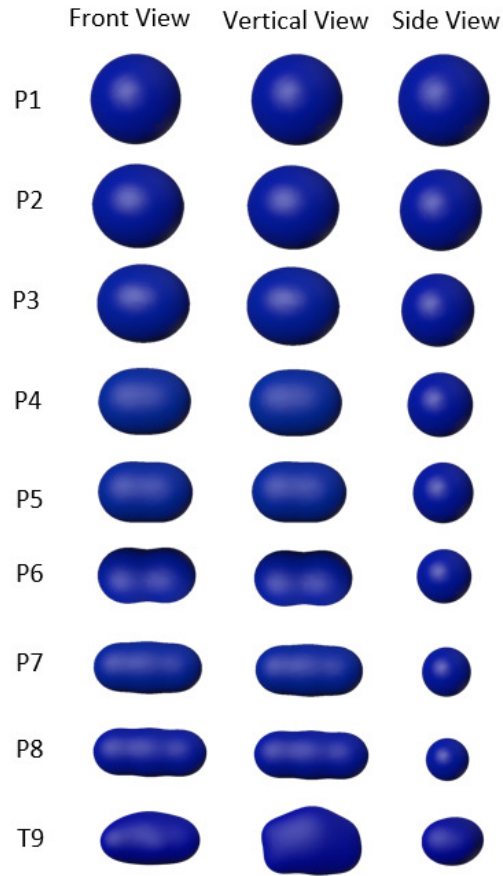
Figure 21: The seven set of particles with stepped morphological parameters.
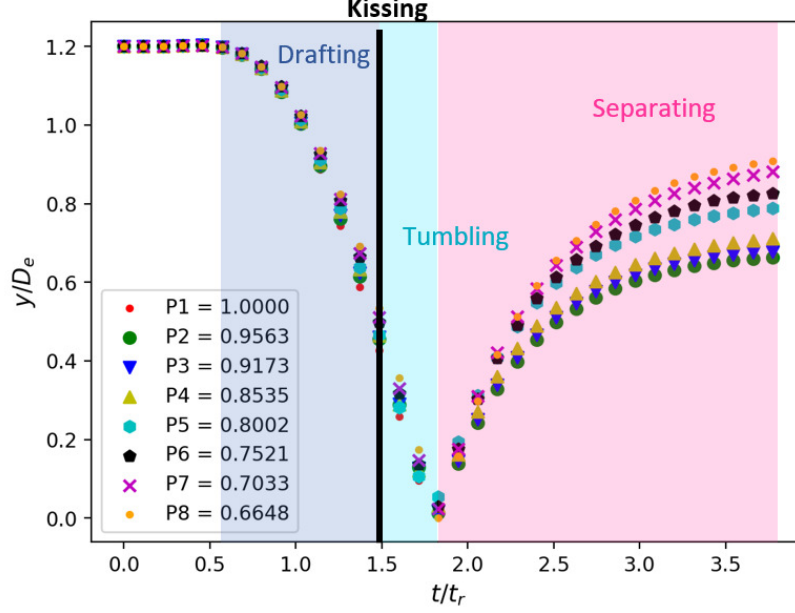
Figure 22: The vertical distance between particles of different morphological parameters, the number in legend stands for CSF value of each particle.

Figure 22 indicates the change of the vertical distance between the leading and the following particles. It can be observed that the CSF is in a negative correlation with the vertical distance between particles during the DKT process. This phenomenon is related to the flow field induced by the morphology and interaction of particles (Figure 23). From flow patterns of P1, P4 and P7, the increase in CSF can obviously enhance the flow field of the following particles and weaken that of the leading particles. Such an impact is more significant in the separation stage. While this correlation is not obvious before drafting and after separating since the particle interaction is not yet formed at that time.

Figure 24 reveals the time series for the vertical velocity and angular velocity magnitude of these studied particles. For settling velocity, it is clear that the decrease in CSF has a negative impact on the settling velocity of both the leading and following particles. As CSF ranges from 0.66 to 1.00, the settling velocity of both particles gradually decreases(Figure 25). This is related to the impact of CSF on the particle flow field. The enhancement in the wake of the following particle leads to a negative impact on the set-
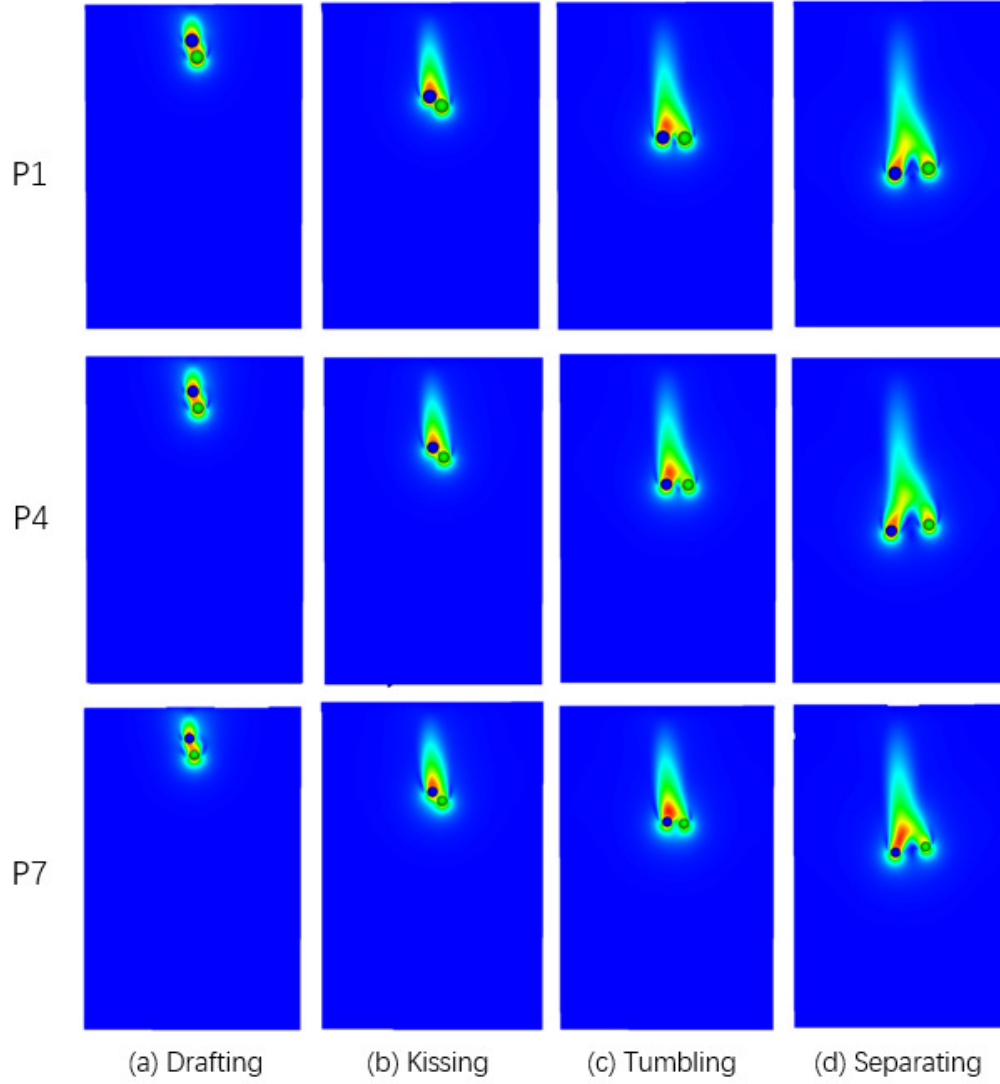
Figure 23: The snapshot of the DKT simulations for P1, P4 and P7 from the side view at the same time-step. Color indicates the fluid velocity magnitude.

tling velocity of the leading particle. It is also known that the particle with lower CSF tends to have larger maximum projected area under the same volume[6, 75]. And the maximum projected area is in negative correlation with the settling velocity. These factors playing together cause the above phenomenon. However, the change in CSF has little impact on the time of peak velocity for pair-particle settling (Figure 26, t_{mU} = the time of peak velocity). For angular velocity, the impact of CSF is obvious on the magnitude (Figure 27). The rotation in DKT problem is mainly caused by particle interaction, which continues throughout the settling. With CSF ranges from 0.66 to 1.00, the magnitude of the leading particles decreases gradually (Figure 27). As for the following particles, the magnitude first decreases then increases. This indicates that the increase in anisotropy degree can lead to a stronger rotation. Surprisingly, the sum of the angular velocity magnitudes for both leading and following particles is about the same, around 0.35 $\pm$ 0.03 $1/s$ in our simulations. This reveals that the overall angular momentum of the pair particles remains basically unchanged. Similar to results of settling velocity, CSF has little impact on the time required to reach the maximum velocity (Figure 28, $t_{m}A$ = the time of maximum angular velocity). Particles with different CSF reach peak angular magnitude basically at the same time. This means that the difference in shapes won't interfere with the rotation sequence of pair-particle settling. In conclusion, particle morphology has a strong impact on the settling dynamics of pair particles. Such impact is not limited in translation but also obvious in rotation. While the settling process is not sensitive to the shape change.

On this basis, we further compare the DKT process of particle pairs P_8 and T_9, which have the same shape features except the sphericity. For settling velocity, obvious difference can be observed on these two particles(Figure 29). Although they share the same CSF and d_n/d_s, T_9 particle pair shows a larger settling velocity and different settling pattern. This phenomenon is mainly caused by the difference in maximum projected area caused by sphericity. The higher sphericity brings more flatness into T_9, which results in larger projected area and higher degree of anisotropy. Note that T_9 particle pair go through an oscillation process during separation, which cannot be observed on the rest particles. This is induced by the interaction from the leading particle to the following one, which makes the following particle deviate from the steady settling state. Together with the flat feature, more rotations are needed to adjust its posture for settling with the maximum projected area. This is in consistency with the results of angular velocity. Figure 30 illustrates
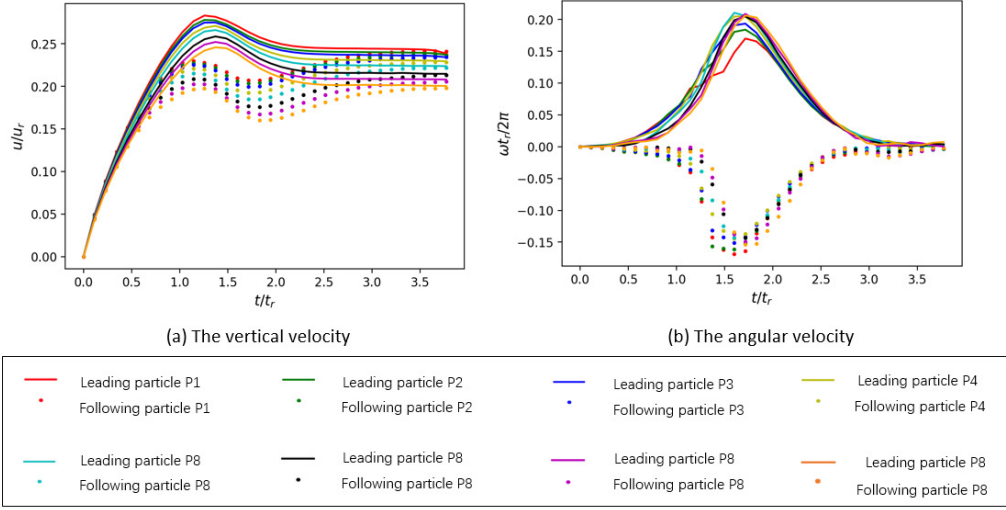
37

(a) The vertical velocity

(b) The angular velocity

Figure 24: The time series of vertical velocity and angular velocity of particle pairs P_1 to P_8.
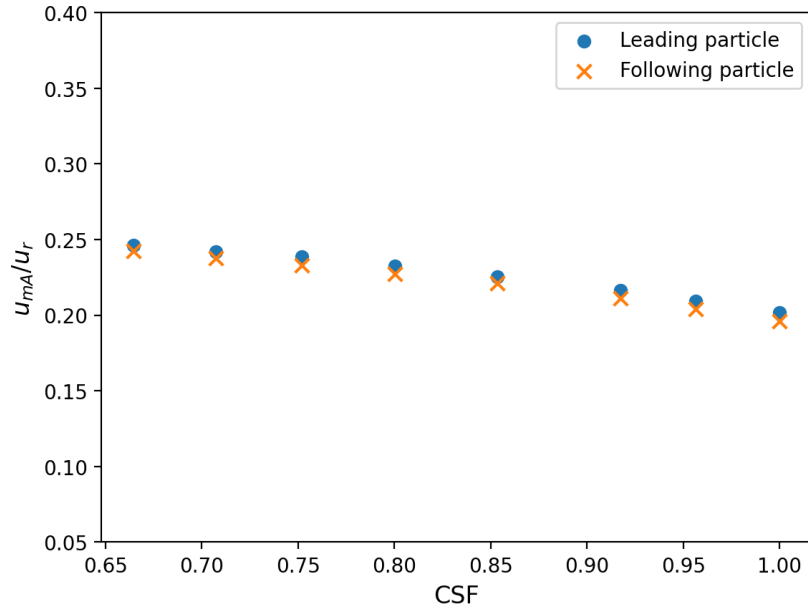

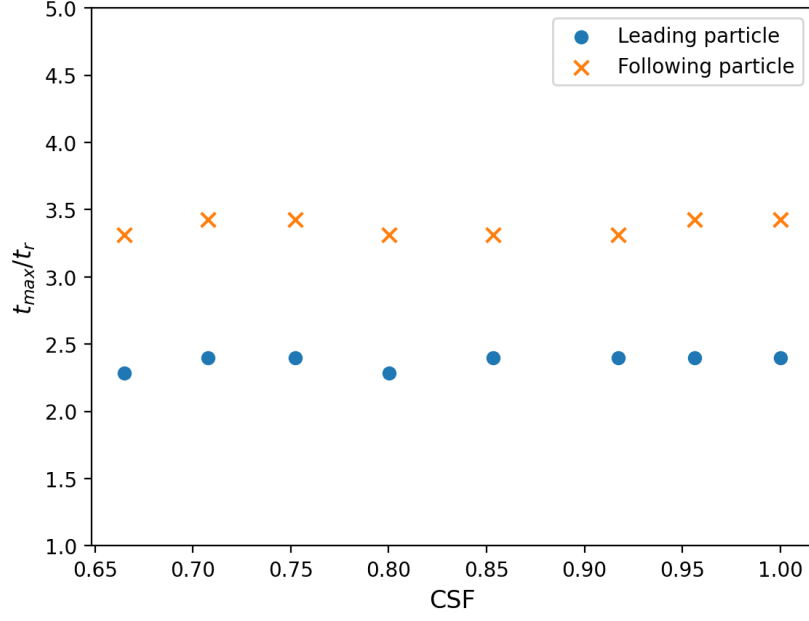Figure 25: The settling velocity of particle pairs P_1 to P_8.

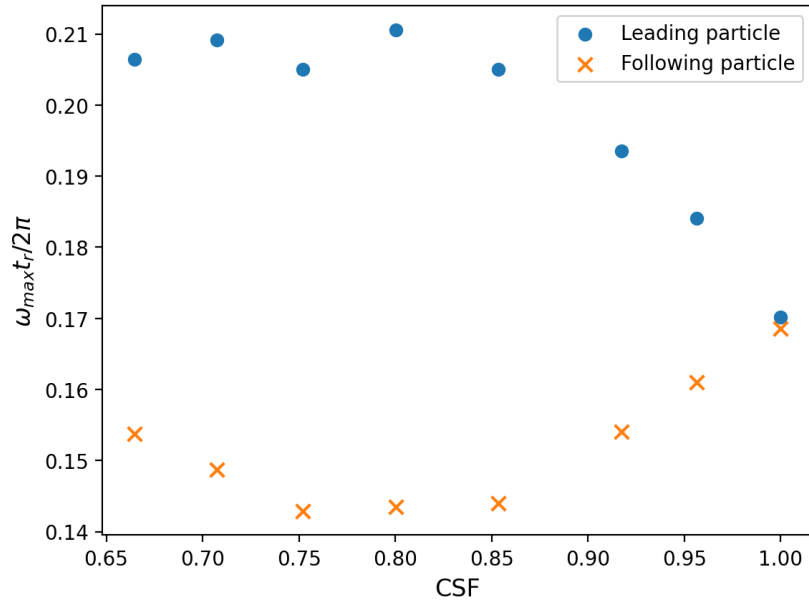Figure 26: The time of peak velocity of particle pairs P_1 to P_8.

Figure 27: The maximum angular velocity of particle pairs P_1 to P_8.
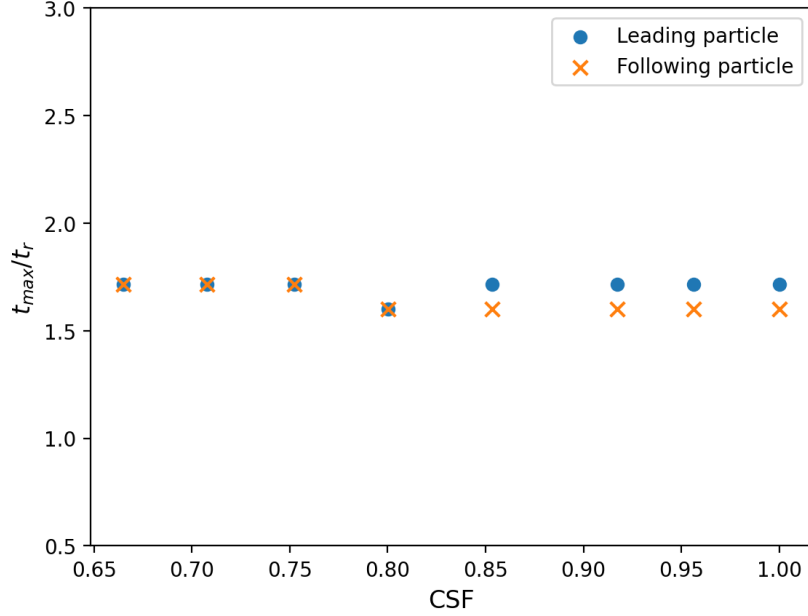
Figure 28: The time of maximum angular velocity of particle pairs P_1 to P_8.

the angular velocities of particle pairs P_8 and T_9. Unlike the others, the T_9 particle pair possesses two velocity peaks. The velocity magnitude of the following particle is also stronger, especially during the separation, which indicates an oscillation process. The above finding further reveals that shape features play an important role in the DKT process and single shape feature is insufficient to characterize such impact. Similarly, a combination of shape features are needed for more practical study.

6. Conclusions

The particle shape has been a crucial factor for the fluid-particle system. To study it quantitatively, we propose the MI-DELBM, which can simulate the fluid-particle system directly with input of XRCT images. Implementations of Metaball-Imaging for avatar capturing and coupled micromechanical models for physical simulations are explained in detail.

To validate the proposed model, simulations of avatars with morphological factors captured from XRCT images of different irregular-shaped particles are carried out on the Jeffery orbit and particle settling experiments without
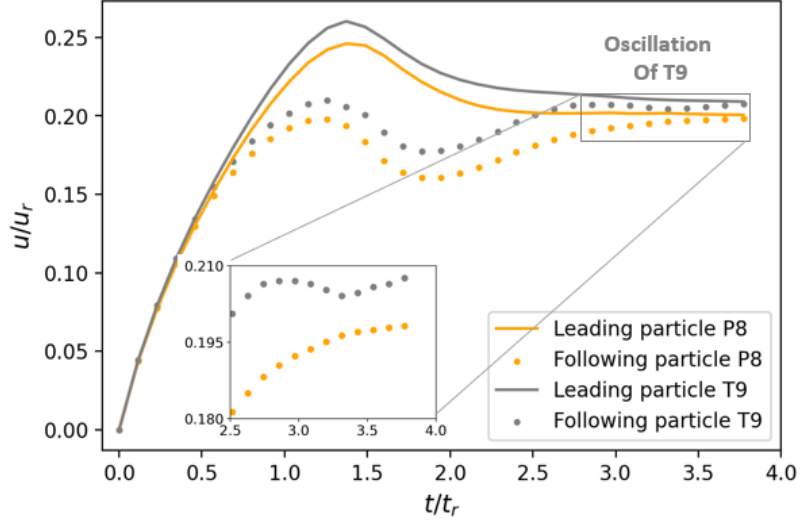
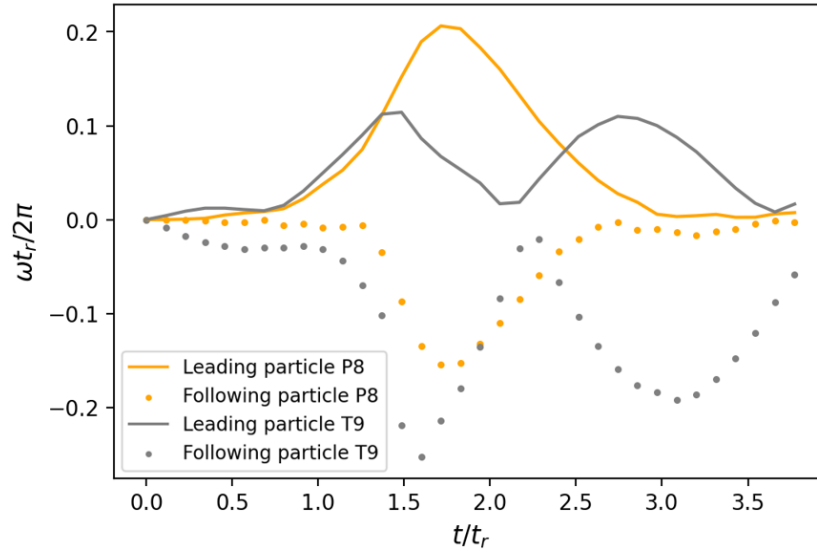Figure 29: The settling velocity of particle pairs P8 and T9

Figure 30: The angular velocity of particle pairs P8 and T9

41

calibration. The comparisons are in a good match. This shows that the MI-DELBM can simulate the particle-particle and fluid-particle interactions of complex shapes accurately.

Finally, we explore the potential of MI-DELBM on the drag and lift forces, as well as the classic DKT process of pair-particle settling with non-spherical particles. Quantitative studies are carried out with selected shape features. On the drag and lift forces, it is observed that the particle shape plays a significant role. These two forces decrease with the increase of Reynold number. And particles with the same circularity could have close drag forces. On the DKT process, It is found that the shape does have a strong impact on the sinking and rotation of particles. This impact focuses on the magnitude of settling and angular velocity. With CSF ranging from 0.66 to 1.00, the peak velocity of leading and following particles increases gradually. As for angular velocity, the magnitude of leading particle first increases then decreases while the following particle shows an opposite behavior. The morphology has little influence on dynamic sequence. All 8 sets of particles reach magnitude of settling and angular velocity at almost the same time.Note that the above two examples both indicate that single shape feature cannot fully reflect the impact of shape on physical processes. A feature combination is needed.

In conclusion, the above results reveal that the proposed MI-DELBM model is an efficient tool to fill the gap between experiments and simulations on fluid-particle systems with realistic, irregular-shaped particles. Potential extensions of it can be found in not only settling behavior in industrial processing but also transportation processes such as pollutant diffusion, dense suspension and drug absorption.

Data Availability

The data that support the findings of this study are available from the corresponding author upon reasonable request.

References

[1] P. R. Robinson, Petroleum processing overview, in: Practical advances in petroleum processing, Springer, 2006, pp. 1–78.

[2] G. Zhao, L. Xiao, T. Peng, M. Zhang, Experimental research on hydraulic collecting spherical particles in deep sea mining, Energies 11 (8) (2018) 1938.

[3] A. Nemmar, P. M. Hoet, B. Vanquickenborne, D. Dinsdale, M. Thomeer, M. Hoylaerts, H. Vanbilloen, L. Mortelmans, B. Nemery, Passage of inhaled particles into the blood circulation in humans, Circulation 105 (4) (2002) 411–414.

[4] J. Cho, H. Y. Sohn, Effects of particle shape and size distribution on the overall fluid-solid reaction rates of particle assemblages, The Canadian Journal of Chemical Engineering 94 (8) (2016) 1516–1523.

[5] G. Bagheri, C. Bonadonna, On the drag of freely falling non-spherical particles, Powder Technology 301 (2016) 526–544.

[6] P. Zhang, S. Galindo-Torres, H. Tang, G. Jin, A. Scheuermann, L. Li, Lattice boltzmann simulations of settling behaviors of irregularly shaped particles, Physical Review E 93 (6) (2016) 062612.

[7] M. Cooley, A. Sarode, M. Hoore, D. A. Fedosov, S. Mitragotri, A. S. Gupta, Influence of particle size and shape on their margination and wall-adhesion: implications in drug delivery vehicle design across nano-to-micro scale, Nanoscale 10 (32) (2018) 15350–15364.

[8] P. J. Withers, C. Bouman, S. Carmignato, V. Cnudde, D. Grimaldi, C. K. Hagen, E. Maire, M. Manley, A. Du Plessis, S. R. Stock, X-ray computed tomography, Nature Reviews Methods Primers 1 (1) (2021) 1–21.

[9] Y. Xiao, L. Long, T. Matthew Evans, H. Zhou, H. Liu, A. W. Stuedlein, Effect of particle shape on stress-dilatancy responses of medium-dense sands, Journal of Geotechnical and Geoenvironmental Engineering 145 (2) (2019) 04018105.

[10] W. Shen, Z. Yang, L. Cao, L. Cao, Y. Liu, H. Yang, Z. Lu, J. Bai, Characterization of manufactured sand: Particle shape, surface texture and behavior in concrete, Construction and Building materials 114 (2016) 595–601.

[11] E. Marteau, J. E. Andrade, An experimental study of the effect of particle shape on force transmission and mobilized strength of granular materials, Journal of Applied Mechanics 88 (11) (2021).

[12] F. Weinhardt, H. Class, S. Vahid Dastjerdi, N. Karadimitriou, D. Lee, H. Steeb, Experimental methods and imaging for enzymatically induced calcite precipitation in a microfluidic cell, Water Resources Research 57 (3) (2021) e2020WR029361.

[13] R. Kawamoto, E. Andò, G. Viggiani, J. E. Andrade, All you need is shape: predicting shear banding in sand with ls-dem, Journal of the Mechanics and Physics of Solids 111 (2018) 375–392.

[14] X. Garcia, J.-P. Latham, J.-s. XIANG, J. Harrison, A clustered overlapping sphere algorithm to represent real particles in discrete element modelling, Geotechnique 59 (9) (2009) 779–784.

[15] C.-Q. Li, W.-J. Xu, Q.-S. Meng, Multi-sphere approximation of real particles for dem simulation based on a modified greedy heuristic algorithm, Powder Technology 286 (2015) 478–487.

[16] X. Nan, J. Hou, Z. Shen, Y. Tong, G. Li, X. Wang, Y. Kang, Cfd-dem coupling with multi-sphere particles and application in predicting dynamic behaviors of drifting boats, Ocean Engineering 247 (2022) 110368.

[17] D. Höhner, S. Wirtz, V. Scherer, A numerical study on the influence of particle shape on hopper discharge within the polyhedral and multisphere discrete element method, Powder technology 226 (2012) 16–28.

[18] B. Yan, R. A. Regueiro, S. Sture, Three-dimensional ellipsoidal discrete element modeling of granular materials and its coupling with finite element facets, Engineering Computations (2010).

[19] R. Regueiro, B. Zhang, F. Shahabi, K. Soga, Micromorphic continuum stress measures calculated from three-dimensional ellipsoidal discrete element simulations on granular media, IS-Cambridge 2014 (2014) 1–6.

44

[20] P. B. Dobrohotoff, S. I. Azeezullah, F. Maggi, F. Alonso-Marroquin, Optimal description of two-dimensional complex-shaped objects using spheropolygons, Granular Matter 14 (5) (2012) 651–658.

[21] S. Galindo-Torres, A coupled discrete element lattice boltzmann method for the simulation of fluid–solid interaction with particles of general shapes, Computer Methods in Applied Mechanics and Engineering 265 (2013) 107–119.

[22] J.-Y. Nie, D.-Q. Li, Z.-J. Cao, B. Zhou, A.-J. Zhang, Probabilistic characterization and simulation of realistic particle shape based on sphere harmonic representation and nataf transformation, Powder Technology 360 (2020) 209–220.

[23] M. Wu, F. Zhou, J. Wang, Dem modeling of mini-triaxial test on soil-rock mixture considering particle shape effect, Computers and Geotechnics 153 (2023) 105110.

[24] K.-W. Lim, J. E. Andrade, Granular element method for three-dimensional discrete element calculations, International Journal for Numerical and Analytical Methods in Geomechanics 38 (2) (2014) 167–188.

[25] M. Wang, Y. Feng, T. Qu, T. Zhao, A coupled polygonal dem-lbm technique based on an immersed boundary method and energy-conserving contact algorithm, Powder Technology 381 (2021) 101–109.

[26] A. Podlozhnyuk, S. Pirker, C. Kloss, Efficient implementation of superquadric particles in discrete element method within an open-source framework, Computational Particle Mechanics 4 (1) (2017) 101–118.

[27] H. Ma, L. Zhou, Z. Liu, M. Chen, X. Xia, Y. Zhao, A review of recent development for the cfd-dem investigations of non-spherical particles, Powder Technology (2022) 117972.

[28] R. Kawamoto, E. Andò, G. Viggiani, J. E. Andrade, Level set discrete element method for three-dimensional computations with triaxial case study, Journal of the Mechanics and Physics of Solids 91 (2016) 1–13.

[29] S. Zhao, J. Zhao, A poly-superellipsoid-based approach on particle morphology for dem modeling of granular media, International Journal for

Numerical and Analytical Methods in Geomechanics 43 (13) (2019) 2147–2169.

[30] D. Peng, K. J. Hanley, Contact detection between convex polyhedra and superquadrics in discrete element codes, Powder Technology 356 (2019) 11–20.

[31] S. Wang, S. Ji, Flow characteristics of nonspherical granular materials simulated with multi-superquadric elements, Particuology 54 (2021) 25–36.

[32] K. Kildashti, K. Dong, B. Samali, An accurate geometric contact force model for super-quadric particles, Computer Methods in Applied Mechanics and Engineering 360 (2020) 112774.

[33] S. Zhao, J. Zhao, N. Guo, Universality of internal structure characteristics in granular media under shear, Physical Review E 101 (1) (2020) 012906.

[34] S. Zhao, J. Zhao, Sudodem: Unleashing the predictive power of the discrete element method on simulation for non-spherical granular particles, Computer Physics Communications 259 (2021) 107670.

[35] Y. Uralsky, Practical metaballs and implicit surfaces, in: Game Developper Conference, 2006.

[36] P. Zhang, Y. Dong, S. Galindo-Torres, A. Scheuermann, L. Li, Metaball based discrete element method for general shaped particles with round features, Computational Mechanics 67 (4) (2021) 1243–1254.

[37] R. Salomon, Evolutionary algorithms and gradient search: similarities and differences, IEEE Transactions on Evolutionary Computation 2 (2) (1998) 45–55.

[38] D. Whitley, A genetic algorithm tutorial, Statistics and computing 4 (2) (1994) 65–85.

[39] S. Ruder, An overview of gradient descent optimization algorithms, arXiv preprint arXiv:1609.04747 (2016).

[40] P. A. Cundall, R. D. Hart, Numerical modelling of discontinua, Engineering computations (1992).

[41] S. Luding, Introduction to discrete element methods: basic of contact force models and how to perform the micro-macro transition to continuum theory, European journal of environmental and civil engineering 12 (7-8) (2008) 785–826.

[42] Y. Peng, L.-S. Luo, A comparative study of immersed-boundary and interpolated bounce-back methods in lbe, Progress in Computational Fluid Dynamics, an International Journal 8 (1-4) (2008) 156–167.

[43] Y. Chen, Q. Cai, Z. Xia, M. Wang, S. Chen, Momentum-exchange method in lattice boltzmann simulations of particle-fluid interactions, Physical Review E 88 (1) (2013) 013303.

[44] E. Lorenz, A. Caiazzo, A. G. Hoekstra, Corrected momentum exchange method for lattice boltzmann simulations of suspension flow, Physical Review E 79 (3) (2009) 036705.

[45] G. B. Jeffery, The motion of ellipsoidal particles immersed in a viscous fluid, Proceedings of the Royal Society of London. Series A, Containing papers of a mathematical and physical character 102 (715) (1922) 161–179.

[46] B. Trevelyan, S. Mason, Particle motions in sheared suspensions. i. rotations, Journal of Colloid Science 6 (4) (1951) 354–367.

[47] E. A. Gaffney, M. P. Dalwadi, C. Moreau, K. Ishimoto, B. J. Walker, Canonical orbits for rapidly deforming planar microswimmers in shear flow, Physical Review Fluids 7 (2) (2022) L022101.

[48] J. V. Roggeveen, H. A. Stone, Motion of asymmetric bodies in two-dimensional shear flow, Journal of Fluid Mechanics 939 (2022).

[49] J. Einarsson, F. Candelier, F. Lundell, J. Angilella, B. Mehlig, Effect of weak fluid inertia upon jeffery orbits, Physical Review E 91 (4) (2015) 041002.

[50] A. Michel, B. Arcen, Reynolds number effect on the concentration and preferential orientation of inertial ellipsoids, Physical Review Fluids 6 (11) (2021) 114305.

[51] M. Ingber, L. Mondy, A numerical study of three-dimensional jeffery orbits in shear flow, Journal of Rheology 38 (6) (1994) 1829–1843.

[52] M. N. Ardekani, P. Costa, W. P. Breugem, L. Brandt, Numerical study of the sedimentation of spheroidal particles, International Journal of Multiphase Flow 87 (2016) 16–34.

[53] W. Fornari, M. N. Ardekani, L. Brandt, Clustering and increased settling speed of oblate particles at finite reynolds number, Journal of Fluid Mechanics 848 (2018) 696–721.

[54] M. M. Mrokowska, Influence of pycnocline on settling behaviour of non-spherical particle and wake evolution, Scientific reports 10 (1) (2020) 1–14.

[55] A. Xu, L. Shi, T. Zhao, Thermal effects on the sedimentation behavior of elliptical particles, International Journal of Heat and Mass Transfer 126 (2018) 753–764.

[56] R. More, M. Ardekani, L. Brandt, A. Ardekani, Sedimentation of spheroidal particles in density stratified fluid, in: APS Division of Fluid Dynamics Meeting Abstracts, 2020, pp. Y05–008.

[57] C. Zhou, J. Su, H. Chen, Z. Shi, Terminal velocity and drag coefficient models for disc-shaped particles based on the imaging experiment, Powder Technology 398 (2022) 117062.

[58] C. Sommer, C. Straehle, U. Koethe, F. A. Hamprecht, Ilastik: Inter-active learning and segmentation toolkit, in: 2011 IEEE international symposium on biomedical imaging: From nano to macro, IEEE, 2011, pp. 230–233.

[59] L. Lei, Y. Seol, K. Jarvis, Pore-scale visualization of methane hydrate-bearing sediments with micro-ct, Geophysical Research Letters 45 (11) (2018) 5417–5426.

[60] V. Angelidakis, S. Nadimi, M. Otsubo, S. Utili, Clump: a code library to generate universal multi-sphere particles, SoftwareX 15 (2021) 100735.

[61] K. Hosseinzadeh, A. Asadi, A. Mogharrebi, M. Ermia Azari, D. Ganji, Investigation of mixture fluid suspended by hybrid nanoparticles over

vertical cylinder by considering shape factor effect, Journal of Thermal Analysis and Calorimetry 143 (2) (2021) 1081–1095.

[62] Y.-M. Chu, S. Bashir, M. Ramzan, M. Y. Malik, Model-based comparative study of magnetohydrodynamics unsteady hybrid nanofluid flow between two infinite parallel plates with particle shape effects, Mathematical Methods in the Applied Sciences (2022).

[63] S. Chen, P. Chen, J. Fu, Drag and lift forces acting on linear and irregular agglomerates formed by spherical particles, Physics of Fluids 34 (2) (2022) 023307.

[64] Z. Fang, Y. Zhang, S. Zhao, X. Li, X. Wu, L. Sun, An experimental investigation on the settling velocity and drag coefficient of micrometer-sized natural, ig-110, ng-ct-10 and a3-3 graphite particles, Journal of Aerosol Science 155 (2021) 105774.

[65] R. Ouchene, Numerical simulation and modeling of the hydrodynamic forces and torque acting on individual oblate spheroids, Physics of Fluids 32 (7) (2020) 073303.

[66] B. J. Connolly, E. Loth, C. F. Smith, Shape and drag of irregular angular particles and test dust, Powder Technology 363 (2020) 275–285.

[67] Y. Wang, L. Zhou, Q. Yang, Hydro-mechanical analysis of calcareous sand with a new shape-dependent fluid-particle drag model integrated into cfd-dem coupling program, Powder Technology 344 (2019) 108–120.

[68] M. Sommerfeld, Z. Qadir, Fluid dynamic forces acting on irregular shaped particles: Simulations by the lattice–boltzmann method, International Journal of Multiphase Flow 101 (2018) 212–222.

[69] Y. Chen, P. Jiang, T. Xiong, W. Wei, Z. Fang, B. Wang, Drag and heat transfer coefficients for axisymmetric nonspherical particles: A lbm study, Chemical Engineering Journal 424 (2021) 130391.

[70] A. M. Bouwman, J. C. Bosma, P. Vonk, J. H. A. Wesselingh, H. W. Frijlink, Which shape factor (s) best describe granules?, Powder Technology 146 (1-2) (2004) 66–72.

[71] L. Wang, Z. Guo, J. Mi, Drafting, kissing and tumbling process of two particles with different sizes, Computers & Fluids 96 (2014) 20–34.

[72] S. Ma, Z. Wei, X. Chen, A systematic approach for numerical research of realistic shaped particle-fluid interactions, Powder Technology 339 (2018) 377–395.

[73] K. Jiao, D. Han, J. Li, B. Yu, Numerical simulations of polygonal particles settling within non-newtonian fluids, Physics of Fluids 34 (7) (2022) 073315.

[74] P. D. Komar, C. Reimers, Grain shape effects on settling rates, The Journal of Geology 86 (2) (1978) 193–209.

[75] J. Liu, P. Zhang, Y. Xiao, Z. Wang, S. Yuan, H. Tang, Interaction between dual spherical particles during settling in fluid, Physics of Fluids 33 (1) (2021) 013312.